UNIVERSITÀ DEGLI STUDI DI PADOVA

Dipartimento di Fisica e Astronomia "Galileo Galilei"

Master Degree in Physics

Final Dissertation

Simulation and tests for the characterization of the response of the detection system fora UAV system

Thesis supervisor:
Dr. Sandra Moretto
Thesis co-supervisor:
Dr. Félix Pino

Candidate:
Vladimir Ruiz

Academic Year 2020/2021

UNIVERSITÀ DEGLI STUDI DI PADOVA

Abstract

Physics Department
Instituto Nazionale di Física Nucleare

Master in Nuclear Physics

Simulation and tests for the characterization of the response of the detection system for a UAV system

by Vladimir RUIZ

The present thesis project consisted in the testing of a gamma rays and neutron detector mounted on an UAV (Unmanned Aerial Vehicle). The detector is a CLLB ($Cs_2LiLaBr_6$), which is a gamma-neutron scintillation detector. This one was tested separately in order to determine its response to different gamma radiation sources (^{137}Cs, ^{60}Co, ^{22}Na, and ^{133}Ba) in different conditions as the change of position of the source respect to the detector (angular variation), and the change of height of the detector respect to a gamma source set on the ground. After the experiments with the gamma sources, ^{241}Am-Be and ^{252}Cf neutron sources were employed in order to test the neutron detection and counting capability of the CLLB. Then, the detection system (CLLB detector + digitizer) was mounted in the drone (UAV) for a simulation of a typical surveillance flight of the UAV, and again to observe and analyze the detection response before a gamma source in motion. For each test with the gamma sources, simulations of the detector and its features were performed with the software GEANT4 in order to compare them with the results obtained experimentally. Additionally, experiments with silicon photomultipliers (SiPM) coupled to CsI and SrI detectors were performed in order to quantify their resolution and compare the values obtained between them, and the resolution values obtained with the CLLB detector.

Acknowledgements

To my thesis supervisors Sandra Moretto and Félix Pino because without their help, support, and patience, this thesis project and results wouldn't have been possible. Also to the Istituto Nazionale di Fisica Nucleare - Laboratori Nazionale di Legnaro (INFN-LNL), for all the resources provided in order to develop this thesis project.

Contents

List of Figures

List of Tables

Dedicated to my parents, brothers, and brothers I met during this master program.

Chapter 1

Introduction

The main component of the detection system of the DRAGON project is the CLLB scintillator detector, as it is the device that will perform the fundamental task of detecting, distinguishing, and counting neutrons and gamma rays. For that reason, this chapter is devoted to the description of the properties and features that an inorganic detector must fulfill in order to be suitable for the tasks that the DRAGON project seeks to accomplish. Additionally, other types or detectors which were also employed in the different experimental tests of this work, are mentioned along with their main characteristics.

1.1 Scintillation Detectors

In order to have a good scintillation material, the following characteristics must be present in it [7]:

- It must be capable to transform the kinetic energy of charged particles into light with high scintillation efficiency.
- The light yield must be proportional to the deposited energy in a range as large as possible (linear conversion).
- The medium must be transparent to the wavelength of its own emission for a proper light collection.
- The decay time of the induced luminescence must be short in order to have fast signal pulses.
- It must have good optical quality and the material should be able to be produced in large enough sizes so it can be practical.
- The refraction index must be very similar to glass (about 1.5) to allow efficient coupling of the scintillation light to a photomultiplier tube (PMT) or other type of light sensor.

Considering the features mentioned before, the most used scintillators are the inorganic alkali halide crystals and the organic-based liquid and plastics. The inorganic scinillators use to have the best light output and linearity, but in general they are relatively slow in their response time. By the other hand, organic scintillators are usually faster but the light yield is less. Also they are applied in different fields; for instance, the high Z value of the components and high density of inorganic crystals favor their choice for gamma spectroscopy, whereas organics are most used for beta spectroscopy and fast neutron detection (due to their high hydrogen content) [7].

In order to address the scintillation process, it is necessary to talk about florescence and phosphorescence. The process of fluorescence is the prompt emission of visible radiation from a material following its excitation by some means, whereas phosphorescence is the

emission of light with longer wavelength than fluorescence, and with a characteristic time that is usually much slower. In addition, delayed phosphorescence produces the same emission spectrum than prompt fluorescence but is also characterized by a much larger emission time following excitation. To be a proper scintillator, the material in question must be able to convert an as large as possible fraction of the incident light radiation energy into prompt fluorescence; reducing at the same time the contributions of both phosphorescence and delayed phosphorescence.

1.2 Organic Scintillators

The fluorescence process in organic scintillators has its origin in the transitions in the energy level structure of a single molecule; hence, it can be observed from a given molecular species independent of its physical state. For instance, anthracene presents fluorescence either as a solid polycrystalline, as vapor or as a part of a multicomponent solution. This feature contrasts with the inorganic scintillators which need a crystalline lattice as a basis of the scintillation process.

An extensive category of organic scintillators is based on organic molecules with certain symmetry properties known as a π-electron structure [7]. The π-electronic energy levels of these molecules are shown in figure 1.1.

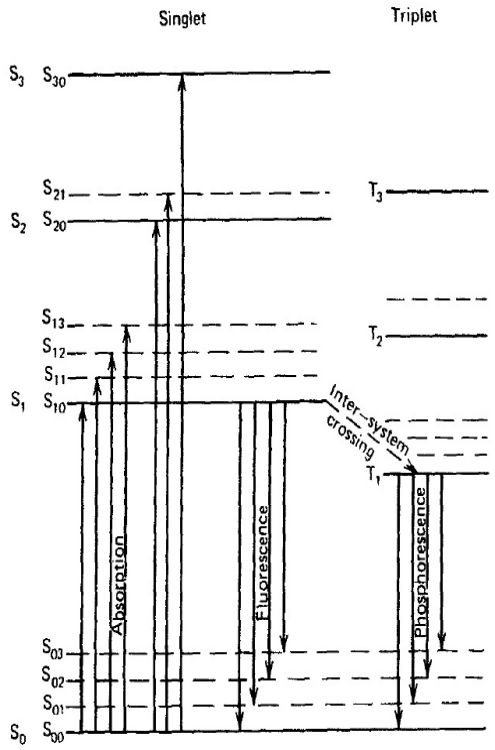

FIGURE 1.1: Energy levels of an organic molecule with π-electron structure.

In the case of the molecules of organic scintillators, the energy gap between S_0 and S_1 is 3 or 4 eV; spacing between higher-lying states is generally smaller. At the same time, each of these electronic configurations is subdivided in levels with much finer spacing. A second subscript is added in order to distinguish these vibrational states. Since the spacing between vibrational states is large compared with thermal energies (0.025 eV), almost all the molecules at room temperature are in the S_{00} state. In the figure 1.1 the absorption of energy

by the molecule is represented by the arrows going up. In the case of a scintillator, these processes represent the absorption of kinetic energy from a charged particle passing close.

The higher singlet electronic states that are excited, de-excitate very quickly (in the order of picoseconds) to the S_1 electron state through internal conversion. In addition, any state with excess of vibrational energy (like S_{11} or S_{12}) is not in thermal equilibrium with its neighbors and also loses the vibrational energy very quick. Hence, the net effect of the excitation process in a simple organic crystal is to produce a population of excited molecules in S_{10} state in a very short time period.

The prompt fluorescence is emitted in transitions between S_{10} state and one of the vibrational states of the ground electronic state. These transitions are shown as downwards arrows in figure 1.1. If τ is the fluorescence decay time for the S_{10} state, therefore the prompt fluorescence intensity at a time t following excitation is given by [7]:

$$I = I_0 e^{-t/\tau} \tag{1.1}$$

In the majority of the organic scintillators, τ is of the order of a few nanoseconds, so the prompt scintillation component is relatively fast.

The lifetime of the first triplet state T_1 is much longer than that of the singlet S_1. Through a transition named *intersystem crossing*, some excited singlet states can be turned into triplet states. The liftetime of T_1 is of the order of 10^{-3} s and the radiation emitted in a de-excitation from T_1 to S_0 is a delayed light emission characterized as phosphorescence. Since T_1 is below S_1, the wavelength of this phosphorescence spectrum will be longer than that for the fluorescence spectrum. Also, in the T_1 state some molecules could be thermally excited back to S_1 state and then decay through normal fluorescence. The processes depicted here represents the origin of the delayed fluorescence observed sometimes in organic scintillators.

The figure 1.1 can be also useful to explain why these scintillators can be transparent to their own fluorescence emission. The length of upward arrows represents the photon energies that will be absorbed strongly in the material. Since all the fluorescence transitions, corresponding to the downward arrows (except $S_{10} - S_{00}$), have a lower energy than the minimum required for excitation, there is very little overlap between the optical absorption and emission spectra (*Stokes* shift), and hence, little self-absorption of the fluorescence. An example of these spectra for the case of organic scintillators appears in the figure 1.2.

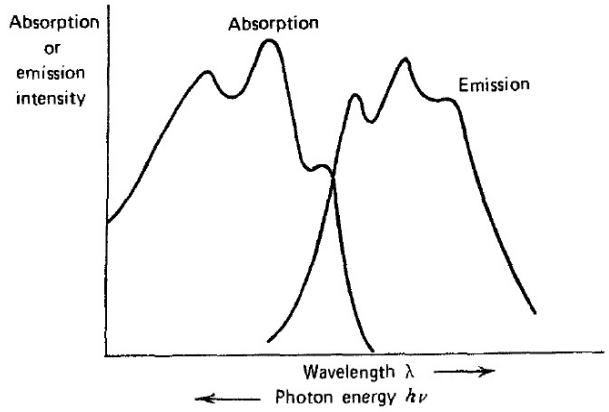

FIGURE 1.2: Optical absorption and emission spectra of a typical organic scintillator.

An important concept in the scintillation process is the scintillation efficiency, defined as the fraction of all incident particle energy which is converted into visible light. Ideally this would have to be as close as much to 1, but there are alternate de-excitation modes of the

molecules which don't involve the emission of light, but the heat production. All these de-excitation processes without emission of radiation are known as quenching. It's important to avoid the presence of impurities in the fabrication process and use of organic scintillators like for instance, dissolved oxygen in liquid scintillators, which degrade the light output providing additional quenching mechanisms.

1.2.1 Some types of organic scintillators

1. Pure organic crystals. The most used are the anthracene and the stilbene. The first one has the highest scintillation efficiency of all the known organic scintillators. By the other side, stilbene has a lower scintillation efficiency but is preferred in experiments where pulse shape discrimination is used to distinguish between scintillations induced by charged particles and electrons. Both of them are relatively fragile and difficult to produce in large sizes. In addition, the scintillation efficiency depends on the orientation of an ionizing particle with respect to the crystal axis. This directional variation (of about 20-30%) affects the energy resolution of the crystals if the incident radiation will produce tracks in many directions inside the crystal.

2. Plastic scintillators. They arise when an organic scintillator is dissolved in a solvent and then is polymerized to produce a solid solution. For example, a solvent of styrene monomer in which a proper organic scintillator is dissolved. The styrene is then polymerized to make a solid plastic. Other plastic matrices can be made of polyvinyltoluene or polymethylmethacrylate. Due to their simplicity of fabrication and manipulation, plastics have become a very useful form of organic scintillators.

   One of the advantage of these scintillators is that they can be shaped in multiple forms and sizes like rods, cylinders, and flat sheets. They also allow to construct large volume solid scintillators due to their accessible price. In these cases, the self absorption of the scintillator light may no longer negligible and it is necessary to pay attention to the attenuation properties of the material.

3. Loaded organic scintillators. They are used generally for the direct detection of fast electrons or alpha particles. They are also adaptable to detection of fast neutrons through the proton recoil process. Nonetheless, there is no photoelectric cross section for gamma rays of typical energies due to the low Z-value of their components (hydrogen, carbon, and oxygen). Hence, typical organic scintillators doesn't show photopeak and only present a Compton continuum in their gamma-ray pulse height spectrum.

   To supply some fraction of photoelectric conversion of gamma rays, there have been attempts to add high-Z elements to organic scintillators. The most usual way is the addition of lead or tin to common plastic scintillators up to a concentration of 10% by weight. It has been proved that tin can be added to liquid organic scintillator solutions in concentrations up to 54% by weight while retaining a low scintillation light output [7]. At low gamma-ray energies, the photopeak efficiency of these materials can be made relatively high. They also have other advantages like fast response and low cost compared with conventional gamma-ray scintillators. The problem with the addition of these high-Z elements is that it causes a decreased light output, and hence, the energy resolution achieved is remarkably lower than that of the inorganic scintillators.

   Other cases of loading organic scintillators are related with the neutron detection. Liquid or plastic scintillators can be introduced with one of the elements with a high cross section for neutrons like boron, lithium or gadolinium. The secondary charged particles and/or gamma-rays produced by neutron induced reactions can be detected directly in the scintillator to produce an output signal.

1.2.2 Response of organic scintillators

1. **Light output**. A small fraction of the kinetic energy lost by charged particles in a scintillator is turned into fluorescent energy. The remaining is turned into heat and lattice vibrations. The fraction of the particle energy that is converted depends on both the type of particle and its energy (scintillation efficiency). For organic scintillators like anthracene, stilbene, and many of the commercially available liquid and plastic scintillators, the response to electrons is linear for particle energies about 125 keV [8]. The response to heavy charged particles like protons or alpha particles will be always less for similar energies and is nonlinear to much higher initial energies. Figure 1.3 shows the scintillation yield of a common plastic scintillator. At energies of few hundred

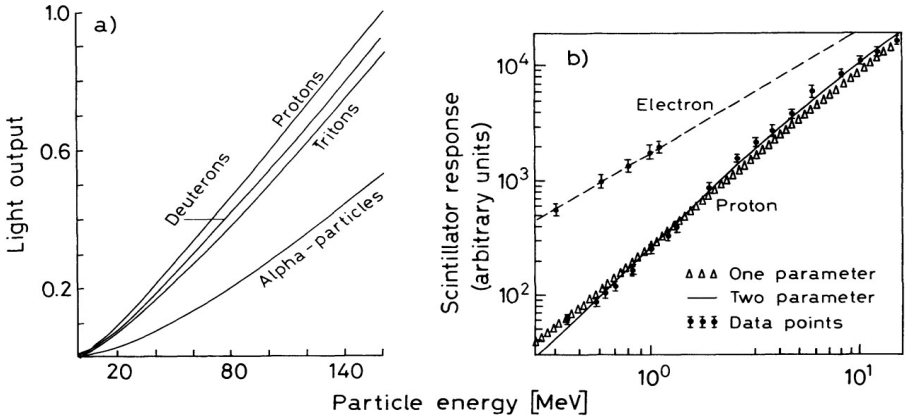

FIGURE 1.3: Scintillation light yield of a common plastic scintillator (NE102) when excited by different particles.

keV, the protons response is smaller by a factor of 10 compared with the light yield of electrons of the same energy. At high energies, the difference is less but the proton response will be always below the electron response. Due to the dependence of the light yield of organics on the kind of particle, there is a nomenclature used to describe the absolute light yield, named MeV electron equivalent (MeVee), which sets the light yield on an absolute basis.

The best way to describe the response of organic scintillators is through the relation between the fluorescent energy emitted per unit path length dL/dx, and the specific energy loss for the charged particle dE/dx. A commonly used relation is based on the assumption of a high ionization density along the track of the particle that produces quenching of damaged molecules and a decrease of the scintillation efficiency. If the density of the damaged molecules along the wake of the particle is directly proportional to the ionization density, it is possible to represent their density by $B(dE/dx)$, where B is a proportionality constant. It's also assumed that a fraction k of these, will produce quenching. Also, it is considered that in absence of quenching, the light yield is proportional to the energy loss [7]:

$$\frac{dL}{dx} = S\frac{dE}{dx} \tag{1.2}$$

where S is the normal scintillation efficiency. To obtain the probability of quenching, from equation 1.2:

$$\frac{dL}{dx} = \frac{S\frac{dE}{dx}}{1 + kB\frac{dE}{dx}} \tag{1.3}$$

equiation 1.3 is known as Birk's formula. The product kB is taken as an adjustable parameter to fit experimental data for specific scintillators [7].

When excited by fast electrons directly or from gamma-ray radiation, dE/dx is small for large values of E and Birk's formula turns to be equation 1.2 [7]. If the incremental light output per unit energy loss is a constant then:

$$\frac{dL}{dE} = S \tag{1.4}$$

which is the regime where the light output is:

$$L = \int_0^E \frac{dL}{dE} dE = SE \tag{1.5}$$

For the case of alpha particles dE/dx becomes too large so the saturation happens along the track and Birk's formula is:

$$\frac{dL}{dx} = \frac{S}{kB} \tag{1.6}$$

Some authors like Clark [7] have compiled a set of data on the absolute scintillation efficiency (S in equation 1.4) of plastic scintillators for gamma-ray excitation. He points out the variability of different measurements made to calculate absolute efficiencies, which in some cases can present a factor of 2 discrepancy. These variations may be in part due to the difference in the purity and past history of the scintillation material. In some organics, the partial overlap of the absorption and emission spectra produce a size dependence of the apparent efficiency for scintillation. Other aspect to consider is prolonged exposure to ionizing radiation, which causes general deterioration of the properties of organic scintillators. It has been observed that plastic scintillators exposed to light and oxygen show a long-term deterioration caused by polymer degradation. In addition, the surface of plastics can suffer crazing caused by exposure to extreme conditions. At the same time, this crazing causes a drop in the observed light output from large scintillators due to the decreased efficiency of internal light reflection.

2. **Time response**. If it's considered that the luminescent states in an organic molecule are formed instantaneously and only prompt fluorescence is observed, the time profile of the light pulse must be a very fast leading edge followed by a simple exponential decay as it's described in equation 1.1. However, a detailed model of the time dependence of the scintillation yield must consider two effects: the finite time required to populate the luminescent states, and the slower components of the scintillation corresponding to delayed fluorescence and phosphorescence. In order to populate the levels from which the prompt fluorescence light arises, times of the order of half a nanosecond are required. For very fast scintillators, the decay time from these levels is only 3 to 4 times greater. The description of the full pulse shape must also include the finite rise time. One model considers that the population of the optical levels is also exponential and the overall shape of the light pulse is given by [7]:

$$I = I_0(e^{-t/\tau} - e^{-t/\tau_1}) \tag{1.7}$$

where τ_1 is the time constant describing the population of the optical levels and τ is the time constant describing their decay. Further observations [7] have lead to the conclusion that the population step is better described by a Gaussian function $f(t)$

with standard deviation σ, so the overall light versus time profile is:

$$\frac{I}{I_0} = f(t)e^{-t/\tau} \tag{1.8}$$

Experimentally, the rise and fall of the light output can be characterized by the FWHM of the resulting light versus time profile, which can be measured using fast timing procedures. The performance of ultrafast organic scintillators is often specified by their FWHM time instead of just the decay time.

3. **Pulse Shape Discrimination**. In most of the organic scintillators, prompt fluorescence represents the majority of the observed scintillation light. Nevertheless, there is a long-lived component observed in many cases, corresponding to delayed fluorescence. The yield curve can be properly described by the sum of two exponential decays (the fast and slow components of the scintillation). Compared with the prompt decay time of the order of few nanoseconds, the slow component has a decay time of hundreds of nanoseconds. Since most of the light yield happens in the prompt component, the long-lived tail doesn't seem to have a great consequence, but it's important because the fraction of light that appears in the slow component depends on the nature of the exciting particle. This property can be used to identify different kinds of particles that deposit the same energy in the detector. This process is known as *Pulse Shape Discrimination (PSD)*, and is often used to eliminate gamma-ray induced events when organic scintillators are used as neutron detectors.

   There is evidence [7] that the slow scintillation component appears with the excitation of long-lived triplet states (T_1 in figure 1.1) along the track of the ionizing particle. Interactions between two such excited molecules can cause that one of them occupies the lowest single state S_1, and the other the ground state. The singlet state molecule de-excites later in the normal way, producing delayed fluorescence. The variation in the yield of the slow component can be explained in part by the differences expected in the density of triplet states along the track of the particle because the bimolecular reaction yield should depend on the square of the triplet concentration. Hence, the slow component fraction should depend mainly on the rate of energy loss dE/dx of the exciting particle and should be greatest for particles with large dE/dx. The current predictions are generally confirmed by measurements of the scintillation pulse shape of many different organic scintillators. In the next chapter, PSD process will be described from the point of view of the processing of the pulses generated by the PMT and their read out made by the digitizers.

1.3 Inorganic Scintillators

1.3.1 Scintillation mechanism in inorganic crystals

It depends on the energy states given by the crystal lattice of the material. As it appears in figure 1.4, electrons have only available discrete bands of energy in materials that can be insulators or semiconductors. The lower band is the valence band, and it represents electrons that are bound at lattice sites. The conduction band represents the electrons that have enough energy to migrate throughout the crystal. Finally, the forbidden band is an intermediate band where electrons can never be present in the pure crystal. The absorption of energy can cause the promotion of an electron from the valence band to the conduction band, leaving a hole in the valence band. In a pure crystal, the return of the electron to the valence band through the emission of a photon is an inefficient process. Additionally,

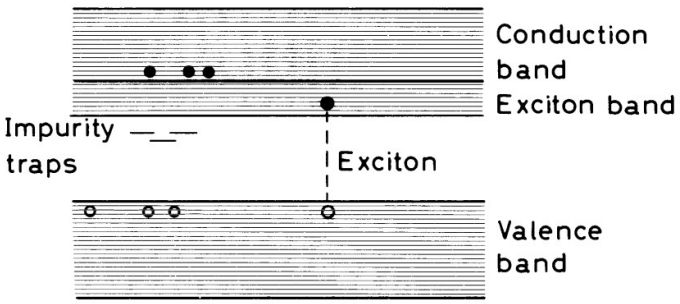

FIGURE 1.4: Energy band structure of a crystalline scintillator.

the width of the gaps is such that the produced photon would has a too high energy to lie in the visible range. So, in order to increase the probability to observe photons in the visible range during the de-excitation process, small quantities of impurities are added to inorganic scintillators. These impurities are known as impurity traps or activators, and they create special sites in the lattice modifying the normal energy band structure of the pure crystal. In consequence, there will be energy states in the forbidden band through which the electrons can de-excitate back to the valence band. Since the energy is lower than the energy of the full forbidden band, the transition now can produce photons in the visible region and works as the origin of the scintillation process. These de-excitation places are known as luminescence or recombination centers, and their energy structure in the crystal lattice defines the emission spectrum of the scintillator.

A charged particle passing through the detection material produce a high number of electron-hole pairs, also known as excitons, created by the promotion of electrons from the valence to the conduction band. The positive hole drifts towards an activator site and ionize it because the ionization energy of the impurity will be less than that of a lattice site. By the other side, the electron is free to move through the crystal until it finds such an ionized activator. The electron can drop into the activator site creating a neutral configuration that can has its own set of excited energy states. If the formed activated state is an excited configuration with an allowed transition to the ground state, its de-excitation will happen very fast and with high probability of the emission of a corresponding photon. If the activator is selected correctly, this transition occurs in the visible energy range. The typical half-lives of these excited states are in a range between 50 and 500 ns [8]. Since the migration time for the electron is much shorter, all the excited impurity configurations are formed at once and will de-excite with the half-life characteristics of the excited state. It's the decay time of these states what defines the time features of the emitted scintillation light. Some inorganic scintillators can be characterized by a single decay time or a simple exponential; however, more complex time behavior has been observed.

There are processes related with the one described. For instance, an electron arriving at the impurity site can create an excited configuration whose transition to the ground state is forbidden, so these states require an additional increment of energy to raise them to a higher state from which de-excitation to the ground state is allowed. A source of this energy can be the thermal excitation, and the resulting slow component of the light is called phosphorescence.

Another possibility is when the electron is captured at an activation site. Some transitions in which no radiation is produced are possible between excited states formed by electron capture and the ground state. In these cases, there is no emission of a visible photon. These processes are known as quenching and represent loss mechanisms in the conversion of the particle energy to scintillation light.

It is possible to make a measurement of the efficiency of the scintillation process from

a simple energy calculation. For many materials, it takes on average about three times the band gap energy to create an electron-hole pair (exciton). For example, in NaI this means that about 20 eV of charged particle energy has to be lost in order to create the pair [7]. For a particle energy of one MeV deposited in the scintillator, an approximate number of 5×10^4 electron-hole pairs are created. Several experimental tests have shown that the absolute scintillation efficiency of NaI(Tl) is about 12% [7]. Then, absorption of one MeV of energy should produce about 1.2×10^5 eV in total light energy, or 4×10^4 photons each one with energy of about 3 eV. Therefore, the yield is very close to one photon per electron-hole pair originally created.

An important consequence of luminescence through activator sites is that the crystal can be transparent to the scintillation light. In the pure crystal, approximately the same energy would be required to excite an electron-hole pair as that liberated when that pair recombines. As a consequence, the emission and absorption spectra will overlap and there will be a considerable amount of self-absorption. Nevertheless, the emission from an activated crystal happens at an activator site where the energy transition is less than that represented by the creation of the electron-hole pair. Hence, the emission spectrum is shifted to longer wavelengths and will not be affected by the optical absorption band of the bulk of the crystal.

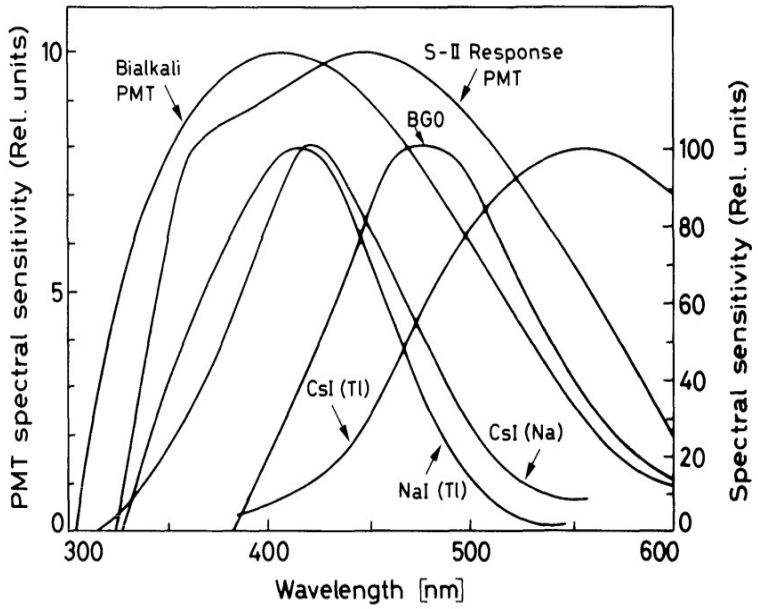

FIGURE 1.5: Emission spectra of many common inorganic scintillators.

In figure 1.5, the emission spectrum of the most commonly used inorganic scintillators is shown. To make use of all the scintillation light, the spectrum must fall near the wavelenght region of maximum sensitivity of the device used to detect light. As reference, the response of many photocathodes are also depicted in the same figure [8].

The main scintillation features of a set of the most common scintillators appear in the table 1.1. The decay times expressed here are approximate since in most of the cases they represent only the dominant decay component. The fifth column shows an estimate of the total number of scintillation photons generated over the whole emission spectrum from the deposition of 1 MeV of energy by fast electrons. The sixth column compares the relative amplitude of the pulse when the scintillator is excited by fast electrons or gamma rays, and coupled to a glass end-window PMT with a bialkali photocathode [7]. For normal inorganic scintillators, the light yield is mostly proportional to deposited radiation energy than is typically observed in organic scintillators. Quenching processes are present here, and they lead

to some non linearity, but in less proportion than in organics. Theres is also variance in light yield for different types of particles of equal energy. Like in the same case of organic scintillators, heavy charged particles generate less light per unit energy. The alpha-to-beta ratio may be much closer to one than in organics.

1.3.2 Characteristics of alkali halide scintillators

CsI(Tl)

CsI activated with Thallium is an alkalide halide that has larger gamma ray absorption coefficient per unite size compared to NaI. Since it is less brittle than NaI, it can be set into more severe conditions of shock and vibration, and is also more soft and malleable. A very useful characteristic of CsI(Tl) is its variable decay time for various exciting particles. Hence, pulse shape discrimination (PSD) techniques can be used to distinguish among various types of radiation. Specifically, it's possible to make very clear distinctions between charged particles like protons or alpha particles in one side, and electron events in the other. This material is less hygroscopic than Na(Tl) but it will deteriorate if it's exposed to water or high humidity.

The emission spectrum of CsI(Tl) has its peak at a much longer wavelength than the NaI(Tl) one (figure 1.5), and it doesn't match so well with the responses of PMTs with S-11 or bialkali photocathodes. This is why the light output is considerably lower in CsI(Tl). By the other side, when measurements are made with photodiodes with extended response in the red region of the spectrum, the scintillation yield is higher than any other scintillator. The absolute yield at room temperature is about 65000 photons/MeV, with a maximum value of 6% higher at -35 °C. The yield falls off with temperature change on any side of this value: to 64% of the room temperature value at -100 °C, and to 95% at 50 °C [7].

The luminescent states in Cs(Tl) are populated through an exponential process that results in an uncommon long rise time of 20 ns for the initial appearance of the light. The posterior decay of these states is one of the slowest for the most used scintillation materials. The light emission for gamma-ray excitation shows two primary components with decay times and relative intensities at room temperature of 0.68 μs (64%) and 3.34 μs (36%) [7].

1.3.3 SrI_2(Eu)

The strontium iodide doped with europium is a novel scintillator material being created as an alternative to lanthanum bromide doped with cerium ($LaBr_3$(Ce)). Gamma-ray spectroscopy of weak radioactive sources needs a large volume of detector materials with high energy resolution. $LaBr_3$(Ce) presents energy resolution of less than 3% at 0.662 MeV, the problem with it is its difficulty to be growth since its crystal structure makes it fragile and easy to break. Furthermore, it presents background radiation due to the presence of ^{138}La, which is undesirable for low count rate applications. The other viable alternative, NaI(Tl), doesn't present intrinsic radioactivity, and it can be produced in large volumes at a a low cost (5 USD per cm^3) [4]. Its disadvantage is that provides poor resolution (about 7% at 0.662 MeV). In contrast, SrI_2(Eu) provides a resolution of 3% at 0.662 MeV, doesn't present intrinsic radioactivity, and offers easier growth compared to $LaBr_3$(Ce).

SrI_2(Eu) crystal provides high proportional light yield (above 80000 photons/MeV), high effective atomic number (Z=49), and easy growth from melt due to its moderate melting point (538°C) and orthorhombic structure that undergoes low thermal expansion between its three crystalline axes, resulting in robust mechanical properties and resistance to cracking [4]. In addition, since the ionic radii of Eu^{+2} and Sr^{+2} are almost identical (1.41 Å and 1.40 Å respectively), there are no observable Eu^{+2} doping gradients in the crystal boule. Hence, it is possible to achieve uniform light yields in large SrI_2(Eu) boules. Finally but not least

important, the main components, strontium and iodine, are very abundant in Earth and non-toxic, and therefore not subject to cost fluctuations or future environmental regulations.

	Wavelength of Max. Emission (μm)	Refractive Index	Decay Time (μs)	Absolute Light Yield (photons/MeV)	Relative Pulse Height with Bialkali PMT
Alkali Halides					
NaI(Tl)	415	1.85	0.23	38000	1.00
CsI(Tl)	540	1.80	0.68 (64%), 3.34 (36%)	65000	0.49
CsI(Na)	420	1.84	0.46, 4.18	39000	1.10
Other Slow Inorganics					
BGO	480	2.15	0.30	8200	0.13
ZnS(Ag)	450	2.36	0.20		1.30
Unactivated Fast Inorganics					
CsI (fast component)	305		0.002 (35%), 0.020 (65%)	2000	0.05
CsI (slow component)	450	1.80	multiple, up to several µs	varies	varies
Ce-Activated Fast Inorganics					
YAG	550	1.82	0.088 (72%), 0.302 (28%)	17000	0.50
LSO	420	1.82	0.047	25000	0.75
A Typical Organic Plastic Scintillator					
NE102A	423	1.58	0.002	10000	0.25

TABLE 1.1: Main features of common inorganic scintillators

Chapter 2

Principles of Detector (CLLB), electronics, DAQ, and Monte Carlo simulations

2.1 CLLB

In the present thesis project, a CLLB ($Cs_2LiLaBr_6$) crystal detector (figure 2.1) was used along with a PMT Hamamatsu. CLLB is a dual mode gamma-neutron scintillator that can replace both high energy resolution gamma-ray detectors and high pressure ^{3}He tubes for neutron detection. The use of pulse height and PSD for neutron detection, combined with a gamma-ray energy resolution better than NaI(Tl) or CsI(Tl), and in the working rate of $LaBr_3$(Ce), make CLLB an excellent alternative for several types of portable instruments like the Spectroscopic Personal Radiation Detectors (SPRDs), and Radionuclide Identification Devices (RIID) [12]. In the table 2.1, there are the main features of the CLLB crystal detector.

Energy Resolution (^{137}Cs)	<4.0%
Density	4.2 g/cm^3
Light output	40000 ph/MeV
wavelength of max. Emission	420 nm
Decay time (γ)	180 ns (61%), 1080 ns (39%)
Decay time (n)	180 ns (50%), 1080 ns (50%)
GRR (Gamma Rejection Ratio)	10^{-7}

TABLE 2.1: Specifications of CLLB detector.

2.2 Electronics

The signals obtained by the crystal scintillator detector were processed by two different digitizers: CAEN DT5725 and Red Pitaya.

2.2.1 Digitizer CAEN DT5725

The DT5725 is a module containing a 8 channel 14-bit 250 MS/s FLASH ADC waveform digitizer with software that allows to select 2 V_{pp} or 0.5 V_{pp} input dynamic range on single ended MCX coaxial connectors. The DC offset is adjustable in the $\pm$1 V (@2 V_{pp}) or $\pm$0.25 V (@ 0.5 V_{pp}) range via a 16-bit DAC on each channel. The ADC resolution and the sampling frequency make this digitizer very proper for mid-fast signal detection systems like liquid or inorganic scintillators coupled to PMT or SiPM. Each channel has a SRAM Multi-Event Buffer divisible into 1/1024 buffers of programmable size. DT5725 is provided with FPGAs

FIGURE 2.1: CLLB detector.

(Field-Programmable Gate Array) that runs DPP (Digital Pulse Processing) PSD firmware for physics applications. The figure 2.2 shows a block diagram of the components of the CAEN digitizer.

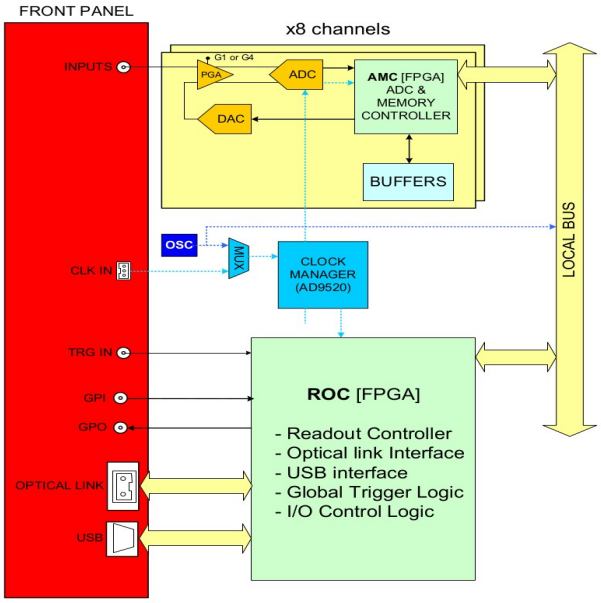

FIGURE 2.2: Block diagram of CAEN DT5725 digitizer.

The mentioned digitizers allow to record the PMT current pulses as digitized wave forms to make subsequent off-line analysis. The installed firmware (Digital Pulse Processing for Charge Integration and Pulse Shape Discrimination DPP-PSD) can pre process data determining the pulses time stamps and integrating them over two gates for the double integration method [9]. All the parameters of the nuclear electronics and data acquisition were controlled through a software called ABCD (Acquisition and Broadcast of Collected Data).

The working principle of each channel in a digitizer where PSD algorithm is implemented is the following: the input signal in the digitizer is continuously digitized and stored

in a buffer. When the signal satisfies the trigger condition (figure 2.3), the analysis algorithm returns over the array according with the pre-gate value, and make the partial (Q_{short}) and total (Q_{long}) integral of the pulse according with the values of the long and short windows. The integrals, time tag, and the desired data of the pulse are stored in an specific array for the data [10]. The detailed parameters to be configured in the implementation of the pulse shape analysis algorithm are shown in figure 2.3. With the integral values it is possible to determine the discrimination parameter (PSD) of each event:

$$PSD = \frac{Q_{long} - Q_{short}}{Q_{long}} \tag{2.1}$$

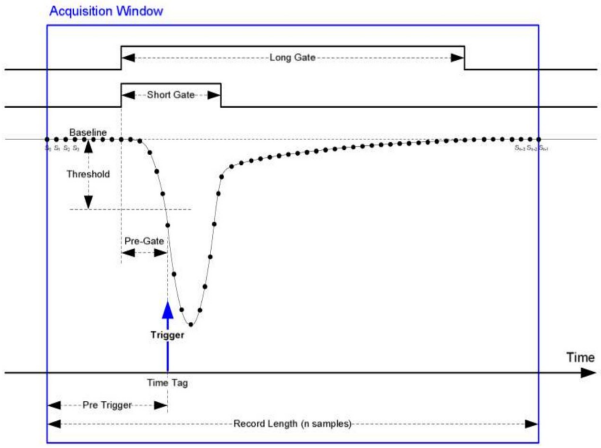

FIGURE 2.3: Acquisition parameters of a typical sample signal.

The PSD parameter represents the delayed fraction of light of the pulse. Among events corresponding to fast neutrons and gammas, it has been observed that PSD parameter values are larger for the neutrons [10].

2.2.2 Digitizer Red Pitaya

Red Pitaya was born as an alternative to expensive laboratory instrumentation. It is known as open source, but the hardware is proprietary. This digitizer is the one that will be actually used in the UAV. It has two 125MS/s RF input and two 125MS/s RF outputs, with 50 MHz analogue bandwidth and 14 bit analog to digital (ADC) and digital to analog (DAC) converters. The software includes oscilloscope, spectrum analyzer, signal generator, LCR meter, and 50 MHz 2x2 MIMO PID controller. It can be reprogrammed to become other devices, as all the IO ports are connected to a common FPGA. There are also auxiliary ADC (250kS/s) and digital IO [11]. The figure 2.4 shows the components of the Red Pitaya digitizer.

It has three USB 2.0 ports, Wi-Fi, Ethernet connector. It uses Linux as operating system. The mass storage device for the operating system is a micro-SD card. Due to the wide bandwidth of the ADC and DAC, the Red Pitaya can be used as a software defined radio receiver and transmitter and in other radio frequency applications [11]. The main features of the digitizers described in the previous sections are summarized in the table 2.2.

2.2.3 High voltage supply

In order to supply the high voltage (HV) to the PMT (1.5 kV approx.), the VME 6U model V6533 unit built by CAEN was used. It has 6 independent channels with an output range between 0 and 4 kV. Three of the channels have positive polarity and the rest have negative

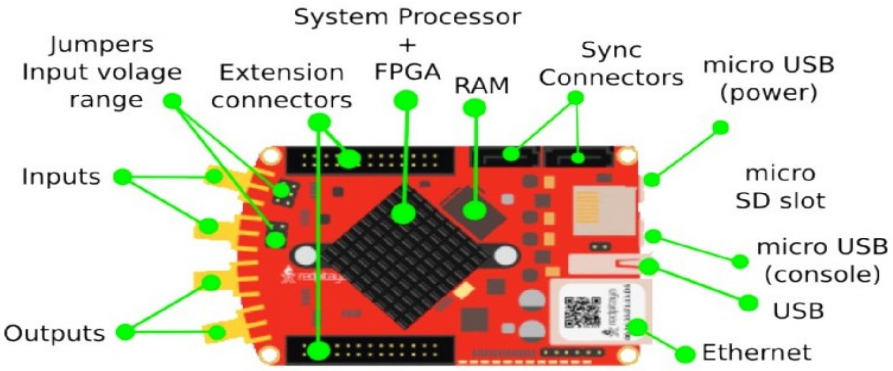

FIGURE 2.4: Components of Red Pitaya digitizer.

Digitizer	CAEN DT5725	Red Pitaya
Dimensions	154x50x164 mm^2	120x25x85 mm^2
Analog Input	8 Ch. (MCX 50 Ω), 0.5 or 2 Vpp, Bandwidth: 125 MHz	2 Ch. ±1 V (LV) and ±20 V (HV). Bandwidth: 40 MHz
Digital Conversion	Resolution: 12 bits, 250 MS/s Simultaneously on each channel	Resolution: 14 bits, 125 MS/s
Memory Buffer	640 kS/ch or 5.12 MS/s Multi-event Buffer 1/1024 buffers	16 kS/ch
Trigger	Individual trigger in each channel	Individual trigger in each channel
Time tag	31-bit counter, 16 ns resolution, 17 s range	-
Interface	USB 2.0 up to 30 MB/s	12C, SPI, UART

TABLE 2.2: Main features of the used digitizers

polarity. It has temperature sensors which allow the continuous monitoring of the unit during its operation. Also, this HV supply counts with a warning signal which alerts if the output voltage has a difference of more than 2% of the programmed voltage. In addition, if the output current is larger than the programmed current, the unit turns off automatically after a lapse specified by the user in the settings of the supply. The V6533 unit is controlled through a software called SHIVA (Software for HIgh Voltage Administration) [10]. The main features of the unit are specified in table 2.3.

2.2.4 PMTs

In many radiation measurements where alpha, beta, X, gamma-rays, and other charged particles are detected, scintillation counters can be used. These counters are coupled to PMTs. A scintillator produces a light pulse as a response to an input radiation; then, the PMT converts this light pulse into an electrical signal.

Output Voltage	0 to 4 kV (SHV conector)
Polarity	3 positive ch, 3 negative ch
Max. Current	3 mA
Max. Power	9 W
Resolution V_{set}/V_{mon}	100 mV
Resolution I_{set}/I_{mon}	50 nA
Precision, VMAX hardware	2% of FSR
Up/Down slope	1 to 500 V/s in 1 V/s steps
Temperature (operation range)	0 to 45°C
Humidity (operation range	0 to 80%

TABLE 2.3: V6533 power supply features

In order to detect light pulses with high accuracy, PMTs need to have high detecting efficiency, wide dynamic range, good time resolution, high stability and reliability, and to operate in environments where high magnetic fields or high temperatures are not present. PMT is a photosensitive device composed by a transparent entrance window, a photocathode, focusing electrodes, an electron multiplier (dynodes), and an anode. All these components are in a vacuum tube [6] (figure 2.5).

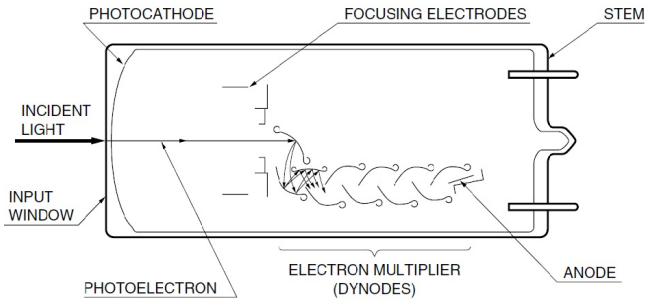

FIGURE 2.5: Cross section of head-on type PMT.

When photons cross the entrance window of the PMT and enter the photocathode, they produce an electron (photoelectron) by compton or photoelectric effect. The photoelectrons are guided by the potential of the focusing electrodes towards the dynodes. Here, the electrons are multiplied by the process of secundary electron emission. The multiplied electrons are collected by the anode, and then they produce an output signal.

2.2.5 Silicon Photomultipliers (SiPMs)

Additionally to the PMTs used in the experiments presented on this project, SiPMs were also part of the experimental setting. SiPM is a solid state silicon detector with single photon sensitivity, and they represent an alternative to PMTs. The main advantages of SiPM are high gain, excellent timing performance, low operative voltage, insensibility to magnetic fields, and high integration level. The specific SiPMs used were the ASD-NUV4S-P-4x4TD, and the ASD-RGB4S-P-4x4TD. Both of them are 4x4 hybrid array of 4x4 mm^2 SiPMs in plastic chip scale package. The detector is completely covered with transparent epoxy layer. The array consists of 16 individual SiPM dies mounted on a single package. A common bias line to the whole array trough the front contacts (cathode for RGB-SiPMs, anode for NUV-SiPMs). Each SiPM is read-out individually from the back of the dies (anode for RGB-SiPMs, cathode for NUV-SiPMs). The array mounts 20-pin, MR-compatible pin-header connectors on the backside [1].

The low afterpulse AdvanSiD NUV-SiPM is based on the "P on N" silicon junction technology for the detection or Near Ultraviolet Light. NUV-SiPmS have their peak efficiency at 420 nm, with detection spectrum between 350 nm to 900 nm. By the other side, the RGB AdvanSiD SiPM hybrid arrays are based on the "N on P" silicon technology for detection of Red, Green, and Blue light. RGB-SiPMs have their peak efficiency at 550 nm with detection spectrum between 350 nm to 900 nm [1]. The main specifications of the mentioned SiPMTs appear in the table 2.4.

Parameter	ASD-NUV4S-P-4x4TD	ASD-RGB4S-P-4x4TD
Effective active area	4×4×16 mm^2	4×4×16 mm^2
Channels (SiPMs)	16	16
SiPM size	4×4 mm^2	4×4 mm^2
SiPM pitch	4.2 mm	4.2 mm
Cell number	9340 /channel	9340 /channel
Array fill-factor	87.30%	87.30%
Cell size (pitch)	40μm × 40 μm	40 μm × 40 μm
Cell fill-factor	60%	60%
Quenching resistance	800 kΩ	550 kΩ
Cell capacitance	90 fF	90 fF
Recharge time constant	70 ns	50 ns
Spectral response range	350 to 900 nm	350 to 900 nm
Peak sensitivity wavelength	420 nm	550 nm
Photon Detection Efficiency	43%	32.50%
Breakdown voltage	Typical: 26 V Min: 24 V Max: 28 V	Typical: 27 V Min: 25 V Max: 29 V
BV standard deviation	50 mV	50 mV
BV uniformity	< 0.4 V	< 0.4 V
Recommended over voltage range	Min: 2V Máx: 6V	Min: 2V Máx: 4V
Dark Count Rate	< 50 kHz/mm^2 @ 2 V OV <100 kHz/mm^2 @ 6 V OV	< 100 kHz/mm^2 @ 2 V OV < 200 kHz/mm^2 @ 4 V OV
Gain	3.6×10>^{6}	2.7×10^6
Breakdown Voltage Temperature Coefficient	26 mV/°C	27 mV/°C

TABLE 2.4: Main features of SiPMs used (NUV & RGB).

2.3 DAQ

The data acquisition system (DAQ) is one of the main components used in nuclear physics experiments. This is in charge of reading-out the ADC results, and also of managing the tasks related with the nuclear detection systems like the HV, power supplies, temperature measurements, and so on. The system used during the experiments of this thesis project presents a novel design in which all the tasks related to the DAQ are divided in several processes. Each process is focused in a simple objective; for example, a process reads the ADC data, another one manages the HV, etc. This DAQ was made for the Rapidly Relocatable Tagged Neutron Inspection System (RRTNIS) of the project entitled "effective Container inspection at BORDer control points" (C-BORD) [5]. The motivation of the project was the high performance needed by the RRTNIS and the requirement of inter-operation with the

project's software infrastructure. The purpose of the C-BORD project is to develop a comprehensive set of technologies to be used together for the Non-Intrusive-Inspection (NII) of commercial freight containers [5].

2.3.1 General structure

The processes, called servers, run independently from each other. Each of them has different connection spots dedicated to the diverse communication possibilities. According to the experimental needs, many configurations can be implemented. Several digitizers can be read in parallel by several servers. Hence, the data collected can be handled by many analysis servers. The figure 2.6 shows a diagram of a DAQ configuration focused on reading data from a single digitizer and controlling the voltage of a single HV supply. Each box represents a process and the arrows represent the interconnections between them.

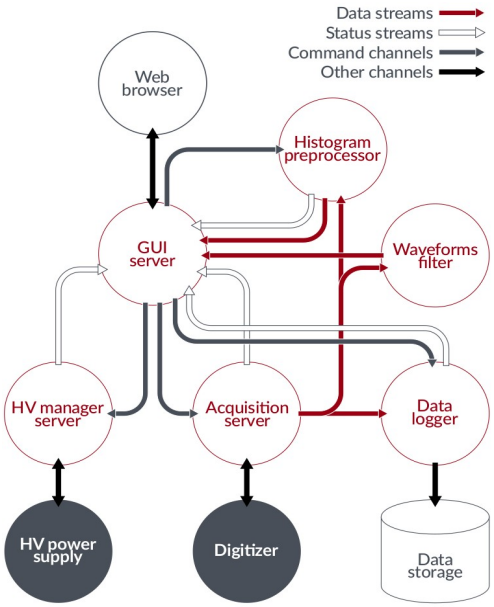

FIGURE 2.6: Configuration of servers and communication channels.

The servers follow a single threaded approach: an event loop reads the current status, performs actions and determines the next state. This approach simplifies considerably the development phase, as the proesses are very light-weight and simple to analyze. The high performance servers were programmed in C++. The system was designed to acquire data from CAEN digitizers, and control CAEN HV power supplies. It's possible to make interfaces with additional hardware by adding suitable new modules.

The communication between processes is obtained through dedicated communication sockets. The implementation lies on the ZeroMQ messaging library, which allows to communicate by means of sending content agnostic messages [5]. The servers can be hosted in the same machine or can communicate through a network. This approach allows to distribute the computational load across different computers in a network. There are three types of communication sockets:

1. Data sockets. They follow the publish-subscribe pattern with a custom binary serialization protocol.

2. Status sockets. They follow the publish-subscribe pattern, with a JSON serialization protocol.

3. Command sockets. They follow the push-pull pattern, with a JSON serialization protocol [5].

A server producing a data stream has a data socket end-point to which several subscribers can connect. With a publish-subscribe pattern, all the messages are duplicated and sent to all subscribers. This pattern allows to carry out different analyses in parallel on the same data-stream. All the servers that generate data streams are designed to be compatible with each other, thus data socket end-points can always be connected together. Digitizer data is serialized with a custom binary format, that reflects the digitizer's data structures.

Status sockets publish messages that describe the servers running status and related information. They follow the publish-subscribe pattern; hence, several subscribers can receive the messages. Also events messages are generated. Event messages announce particular events that happen in the server, for instance an acquisition start, or a digitizer malfunction. Command sockets follow a push-pull pattern that guarantees messages delivery. Several servers may send commands to a single receiver. Status data and commands are serialized as JSON strings [5]. JSON serialization was selected for its simplicity and great support across the programming languages. Configuration files are written as JSON objects as well and therefore can be updated over the network.

2.3.2 Binary protocols

Data sockets deliver the digitizer data as binary messages with two different protocols. CAEN digitizers record signal waveforms and provide them as buffers of 16 bits integers. Some additional waveforms can be added to the buffers which show integration gates and other information regarding the internal operation of the firmware. Signal waveforms are recorded with a 14 bytes header that contains a 64 bits timestamp, a 8 bits channel number, a 32 bits number describing the number of samples in the waveform, and finally a 8 bits number describing the number of optional gate waveforms. The signal waveform follows as a buffer of 16 bits integers. The optional gates follow as a sequence of buffers of 8 bits integers. CAEN digitizers with a Digital Pulse Processing (DPP) firmware with Pulse Shape Discrimination (PSD), produce data that is pre-processed. They can still provide waveforms but also signal integrals over two different integration gates (a short and a long one). Events are serialized as 16 bytes words that contain a 64 bits timestamp, a 16 bits integral on a short gate, a 16 bits long integral, a 16 bits integer with the baseline of the event, a 8 bits channel number, and finally an unused 8 bits word (figure 2.7) [5].

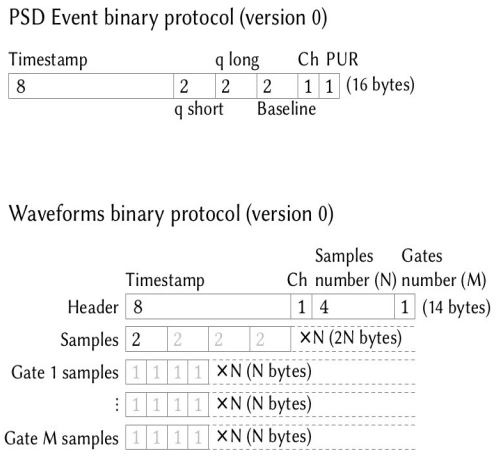

FIGURE 2.7: Binary protocols for digitized data.

2.4 Monte Carlo Simulations

Simulations based on Monte Carlo methods are used to solve complex problems of math, physics and many other fields of science in which there are models with many independent variables involved. In these cases, exact solutions methods or other calculation methods, including computational methods, are not efficient to address them. In the case of the transport of radiation through matter, this was addressed with the Boltzmann's transport equation [10]. Nevertheless, this method is not successful when it's applied to a system with finite geometry. Hence, at the end of 1950s Monte Carlo method applications were developed with the help of computers in order to solve this problem.

The method looks for a numerical solution to a problem which models objects interacting with each other or with their neighborhood environment with basis on object-object and object-environment interactions. So for the case of the transport of radiation through matter, detailed simulations where the experimental interactions of a particle are given in a sequential order represent an exact solution of the transport equation. The solution is only affected by the uncertainties that are inherent to the statistical nature of the interaction between radiation and matter.

In Monte Carlo simulations for transport of radiation, the history of a particle is a random sequence of free steps interrupted by interactions which produce effects like changes in its direction of motion, energy loss, and sometimes, the production of secondary particles. In order to simulate this histories, it's necessary to know the interaction modes of the particle, which is the set of differential cross sections of the relevant mechanisms of interaction. For instance, in the case of gamma-rays with an energy range from tens of keV to units of MeV, the most relevant interaction mechanisms are the photoelectric effect, Compton effect, and the creation-annihilation of e^--e^+ pairs.

The differential cross sections determine the probability density functions of the random variables that depict a history [10]. Among these variables are the mean free path between successive interactions, the kind of the interaction, the energy loss, the angular deflection of a particular event, the initial state of a secondary particle, etc. Once the probability density functions are known, the random histories can be produced applying the proper sampling method. The main idea is to produce a large enough number of histories to obtain precise information about a particular experiment.

In the present thesis research, Monte Carlo simulations of transport of neutrons and gamma-rays through matter (detectors) were performed. The purpose of these simulations were to analyze more deeply some features of the CLLB detector like the efficiency for gamma-rays in different physical conditions for the detector (different positions of a radioactive source respect to the detector) and the spectra generated by the radiation of these sources when it interacts with the detector. The GEANT4 code was used in order to perform all of these simulations. This code is widely used to reproduce phenomena in the field of experimental nuclear physics. The simulations were compared with the experimental results in order to have in advance an idea of what would be expected to obtain in every specific experimental test.

The general procedure used to perform the Monte Carlo simulations with the GEANT4 code was:

- **Define the geometry of the experiment.** The geometry and chemical composition of every element interacting with the radiation were defined. In this case, the cylindrical CLLB detector inside the aluminum cylindrical cover. The figure 2.8 shows the CLLB detector in blue inside the aluminum cover shown in transparency in gray. It's important to mention that neither the PMT nor the optical coupling appear here because the simulations just include the energy deposition processes (neutrons and gamma-rays) in the sensitive volume of the detector (scintillator). The dimensions of the CLLB

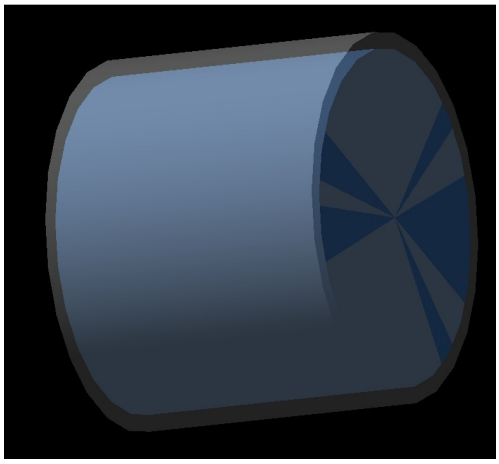

FIGURE 2.8: CLLB detector inside aluminum cover.

detector are 2 in (50.8 mm) of diameter, and 2 in of height. The detailed dimensions of both the CLLB and the aluminum cover are shown in figure 2.9. As a reference, a

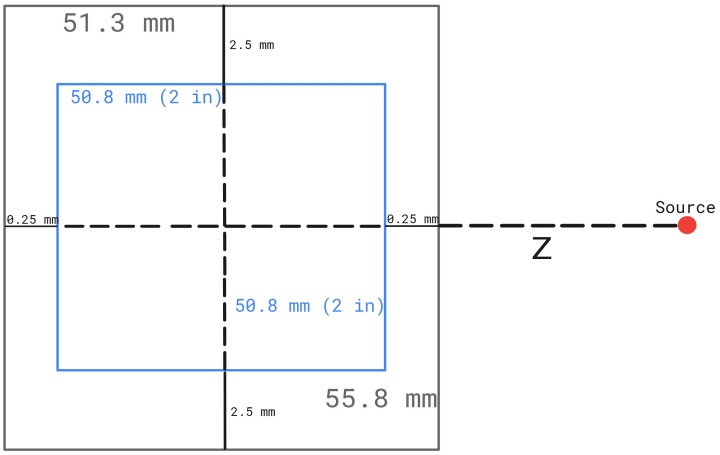

FIGURE 2.9: 2D diagram of Detailed dimensions of CLLB inside aluminum cover.

source was set to indicate the front face of the detector, and the axis used in the simulations to set the distance between the source and the frontal face was indicated. It's important to mention that regarding the simulations in Geant4, the origin of the system changed since the 0.25 mm between the CLLB and the aluminum of the left part of the diagram were increased to 0.5 mm in order to have the CLLB at the right edge and was in fact the first object interacting with the radiation produced by the sources.

- **Description of the primary particles source.** In the simulations the sources employed produced monoenergetic gamma-rays and were punctual and isotropic. For the experimental tests presented in this work, the sources simulated were ^{137}Cs, ^{22}Na, ^{60}Co, ^{57}Co, and ^{133}Ba.

- **Description of the physical processes implied in the experiments.** For the current tests, these are the interactions of the mentioned gamma sources with the material of the detector.

- **Determine the information to obtain from the simulations.** The objective of the set of simulations performed was to obtain the efficiency of the main gamma peaks (peak

efficiency) that characterize each one of the used sources. These efficiencies were compared to the ones obtained experimentally from the gamma peaks of each source so it was possible to determine in advance the behavior of the detector in response of the incident radiation.

2.4.1 GEANT4

In order to perform all the mentioned simulations, the software GEANT4 was used in the present project. This is a widely used tool in particle and nuclear physics for simulating the transport of radiation through matter. It is based in object-oriented technology, and implemented in the programming language C++. It emerged in 1993 as a collaboration of scientists and engineers around the world. GEANT4 offers an extensive variety of particles, physical processes and models, materials, and tools that allow to handle complex geometries in an energy range between 250 eV to few TeV [10].

The main feature of GEANT4 is the clarity in which physical processes are used along the models which describe them. In GEANT4 the models are based on experimental data, theoretical models, and parametrizations. The user must indicate the physical processes to be analyzed, and their corresponding models, respect to the features of the phenomenon being studied like the type of particle that is being simulated, the range of energies, the materials composing the geometrical model, what information will be obtained from the simulations, etc.

In GEANT4, the geometrical model is built in the class *G4VDetectorConstruction* from the use of the concepts of logical and physical volumes. The first one represents an element of the geometry with a particular shape, and it can contain other volumes. The second represents a spatially positioned logical volume inside another volume (logical) denominated *mother volume*. In the present project, the logical volumes were build using the concept of *Constructive Solid Geometry (CSG)*, which consists in defining homogeneous solids with different shapes (cylinders, cubes, spheres, etc.) separately. Then, these volumes are set properly in order to reproduce the geometrical model to study, in this case this was the CLLB detector inside the aluminum cover (figure 2.8).

To generate the primary particles, GEANT4 uses the class *G4VUserPrimaryGeneratorAction*, which specifies the characteristics of the particle (position, time, kinetic energy, angular distribution, etc.). In the current case, the class *G4GeneralParticleSource (GPS)* was used to produce sources of complex primary particles in a simple way. To achieve this, an input file with all the necessary commands to describe the primary particle source was created. The features that can be set with the GPS class are the spatial distribution (point-like, 2D, 3D, etc.), angular distribution (unidirectional, isotropic, conic), energy (monoenergetic, continuous or discrete spectra), the number and type of particles to generate in each event.

The class *G4UserPhysicsList* is used to define the particles and physical process involved in the case. Since in this project gamma photons in an energy range between hundreds of keV and 1.5 MeV were simulated, the physical processes of interest are the photoelectric effect, the Compton effect, and the creation-annihilation of e^--e^+ pairs. The class *G4Step* was used to extract the energy deposited in the scintillator by the gamma photons. At the end of each event, a histogram with the data generated was built. The histogram represents the light emission spectrum corresponding to the incident beam of gamma photons.

Chapter 3

DRAGON (Drone for RAdiation detection of Gammas and Neutrons) Project

3.1 Motivation and objective

The DRAGON Project emerges as a response of potential threats to public health and homeland security caused by radioactive and nuclear materials. Such threats can be for instance terrorism menaces, lost of orphan sources, nuclear accidents or radioactive contamination. Therefore, the capability to survey large areas quickly in case of radiation leakages and/or nuclear disasters is fundamental. The DRAGON project provides a fast and safe method of search of nuclear contamination. The main features of this system is the capability of distinguish between neutrons and gamma radiation, and its compactness and mobility which allow autonomous measurements and navigation which in turn provides a detailed description of the radiation levels or contamination in the surrounding area.

The DRAGON project purpose is to design, develop, and characterize a mobile system composed by an Unmanned Aerial Vehicle (UAV). This vehicle contains a detection system capable of sensing radioactive contamination spread on an area as large as some tens of square meters. In order to detect and distinguish between neutrons and gamma radiation, this technology includes thermal and fast neutron detectors together with gamma-ray detectors. The measurements are complementary, so is expected that their combined efficiency improves the detection performance. One of the challenges of the system is to detect Special Nuclear Materials (SNM) such as Highly Enriched Uranium and Plutonium. This is because these materials can be easily masked or shielded. Hence, both neutrons and gamma rays emitted by SNM have to be detected for increasing the sensitivity against the natural background.

3.2 DRAGON structure: detectors and UAV

In terms of the detection system, an ideal configuration would use a large volume and a very high density material for the high counting rate. This guarantees a high stopping power of the radiation, which translates in a high probability of stopping and detecting radiation. The challenge with such setting would be coupling the detector on a UAV. There have been several candidates for these conditions including Geiger-Müller (GM) tubes, cadmium zinc telluride detectors (CZT), semiconductor detectors, and scintillator detectors such as $LaBr_3$(Ce), NaI(Tl), and CsI [2]. They are focused mainly in the detection and identification of gamma radiation sources but not the neutron radiation as such. In particular, the GM tubes are used for dosimetry purposes, while the CZT detectors are employed for identification of radionuclides (spectroscopy). Nevertheless, both devices have very low sensitivity,

being lightweight (low electronic density for the GM tubes) or of small volume (about 1 cm^3 for CZT) [9].

In the case of scintillators, small and medium size ones have been used because they give the possibility to perform dosimetry and spectroscopy measurements at the same time. The medium size scintillators have sensitivity considerably higher than GM tubes and CZT detectors. Nevertheless, the increase of size and weight of the UAV payload translates in more power consumption, and hence, in less flight time or more powerful motors. In many cases, NaI(Tl) detector is a very good candidate to perform gamma spectroscopy in field applications due to its affordable price and characteristics (robust, high electronic density, high light output, linearity, etc.) that make it get a good gamma response. The problem with this detector is its low neutron sensitivity. By the other side, there are new plastic scintillators (like the EJ-276 from Eljen Technology) with very good gamma/neutron discrimination capabilities but their gamma response is inadequate in order to perform spectroscopy in a straightforward way [9].

Considering all the features stated previously about the many kinds of detectors, the Li containing elpasolite scintillators (CLYC, CLLB, etc.) turn out to be the best option to fulfill the requirements mentioned before. They present excellent energy linearity, high light output (good energy resolution), good thermal neutron efficiency through the $^{6}Li(n,\alpha)^{3}H$ capture reaction [9]. An important characteristic of the La containing scintillators like CLLB, CLLBC, $LaBr_3$, etc. is that they exhibit an intrinsic radioactive background from naturally occurring ^{138}La and from alpha decays from ^{227}Ac contamination [9]. In the framework of the DRAGON project, the current work presents studies of the response of a CLLB middle size scintillation detector, to gamma and neutron radiations in similar physical conditions to those of a tracking flight of the UAV. In the figure 3.1 at the left, appears the prototype of the detection system which is composed by the CLLB detector itself, the digitizer (Red Pitaya), a mini computer for the data analysis, and the high voltage power supply; and at the right, the actual designed cover with the CLLB and the digitizer inside of it.

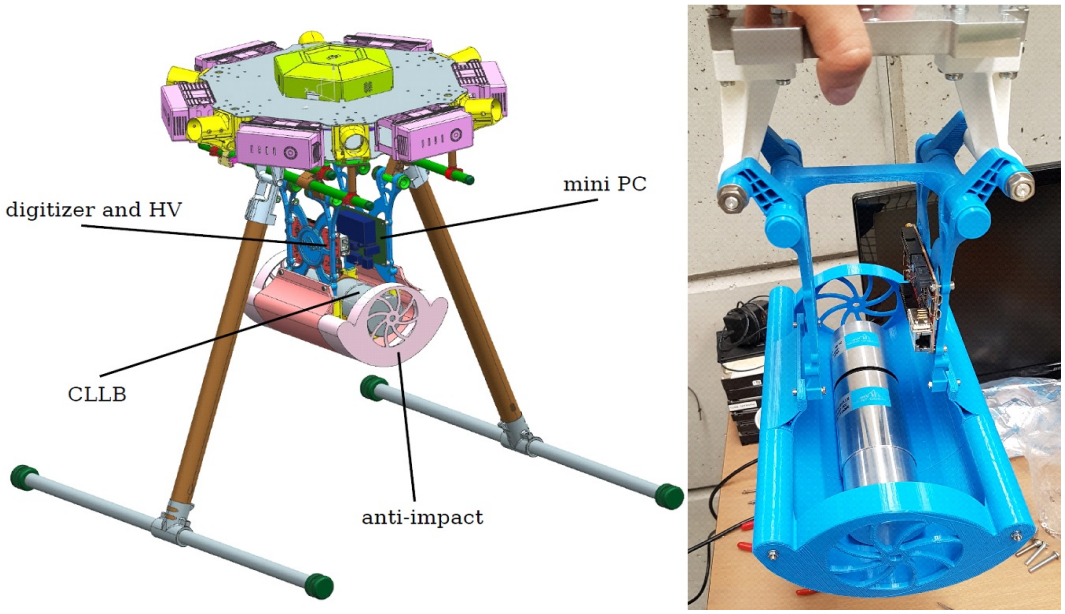

FIGURE 3.1: Prototype of the detection system which will be mounted in the UAV (left); Actual design (right).

The main advantage of the UAV is that can be used in severe scenarios when the radiation doses are too high for a human safety or if the place where the accident happened is difficult to access. There are many designs of UAV, like a fixed-wing UV or single rotor

helicopter-style aircraft. The task of the UAV is to supply fast data acquisition and to create a precise map of the area of interest. Taking these factors in consideration, a hexa-copter or a quad-copter gives the highest flexibility in terms of position precision.

The DRAGON project considers the standards describing the requirements for mobile systems, including the ANSI N42.43. Since it's pretended that the system be used in potentially contaminated areas, it is necessary to perform experimental tests with relevant gamma and neutron sources to satisfy the IAEA requirements for safety and security in the field.

An important issue about the project is the miniaturization of both the detectors and the electronics on board the drone. The design of the UAV is in the figure 3.2. The subsystems

FIGURE 3.2: Design of UAV for DRAGON project.

that compose the assemble of both the drone and detectors are depicted in the figure 3.3 [2]. Functionally, the UAV provides an autonomous real time path planning, and a flight controller to allow pilot the drone manually. It also incorporates a telemetry communication using a dedicated 2.5 GHz radio link.

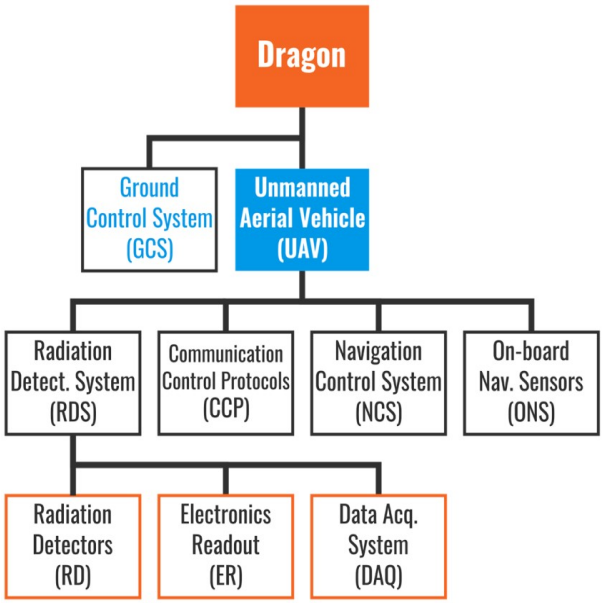

FIGURE 3.3: Components of the DRAGON project.

The Radiation Detection System (RDS) uses two detection solutions: the first one is a radioactivity counter monitor consisting in a plastic scintillator EJ276 (Excellent physical hardness, Long-term stability of scintillation and optical characteristics); the second is a radionuclide identification system consisting in a gamma spectroscopic scintillator with thermal

neutron detection capability (CLLB) [2]. Both solutions are designed to be interchangeable with the same electronics readout. This is possible due to the suitable mechanical design thought to adapt the system to the requirements of a variety of threats in nuclear security. The first solution is used as a radioactivity counter, while the second one works as a second-line identification system. In addition, the second solution can be employed as a first-line inspection system in cases of very high dose environments, like the ones involving high quantities of neutron emitting materials. In order to detect the scintillation light signal, both solutions use standard PMT. There is also an alternative readout channel based on large area SiPMs with the objective of reducing overall weight, size and power consumption of the detection system.

A 125 MHz digitizer (Red Pitaya) is mounted on the UAV to complete real time wireless measurement. To reduce energy consumption, the sampling rate was reduced. This can be compensated in part by increasing the number of resolution bits up to 14 [2]. The digitizer is controlled by a FPGA to get the necessary speed for the detection and signal processing, and improve the efficiency of the reader. This combination makes possible to install an embedded operating system like Linux, capable to run the required software for the data acquisition (DAQ). The integrated FPGA executes the data preprocessing efficiently and serves it directly to the CPU. This hybrid solution makes easier the development efforts since only the FPGA is in charge of the high performance data processing. By this way, the total processing time for a radiation detection event should be at much 10 μs to allow the acquisition of approximately 10^3 events/s [2].

The selection of the UAV frame is fundamental because it defines the stability in wind conditions and the maximum weight the drone can carry, specifically with the used Radiation Detection System which weights a little more than 2 Kg. For reasons of completeness, a 6-propeller frame was used with 750 KV brush-less motors, and 50 A motor controller [2]. The flight controller employed is the Pixhawk, and a quadcore processor-based companion board was used for the measurements. In addition, the board controls the flight parameters acting as a link between the Ground Control Station (GCS) and the drone using a WiFi link, and it also interfaces the sensors, streaming the data to the GCS. The nominal cruise speed of these applications is in a range between 10 Km/h and 40 Km/h. The interface of the RDS is a Linux based operating system capable of managing multiple processes like the flight control [2].

Chapter 4

Radionuclide identification system based on an inorganic scintillator (CLLB)

The experiments developed during this project are focused on the analysis of the response of the CLLB detector to neutrons and gamma radiation. This chapter contains the analysis of the CLLB detector in terms of energy resolution, time resolution, the high rate dead time of the digitizers (Red Pitaya respect to to CAEN), the efficiency of the detector respect to the position (angle) change of the radioactive source, the neutron detection, and capacity of the detector using the Red Pitaya digitizer (since this is the one that will be on board of the UAV). For the gamma radiation, the radioactive sources were: ^{133}Ba, ^{60}Co, ^{22}Na, and ^{137}Cs; and for the neutrons: ^{252}Cf and an ^{241}Am-Be mixed source. Regarding the tests with the neutron sources it's important to mention that it was observed that the CLLB detector is also able to detect fast neutrons. These results are also included in this chapter.

4.1 Optimization of Q_{short}, and Q_{long} for the best Figure of Merit (FoM)

Before starting to make the whole sets of measurements that characterize the detection capabilities of the CLLB detector, it was necessary to optimize the parameters of the digitizers in order to get the best responses. This means that, since the PSD was the method used to discriminate between gamma photons and neutrons, the Q_{long} and Q_{short} (equation 2.1) parameters need to be optimal (recall that the Q parameters are the integration windows, these can be observed in figure 4.1). In other words, Q_{long} and Q_{short} must be selected in such a

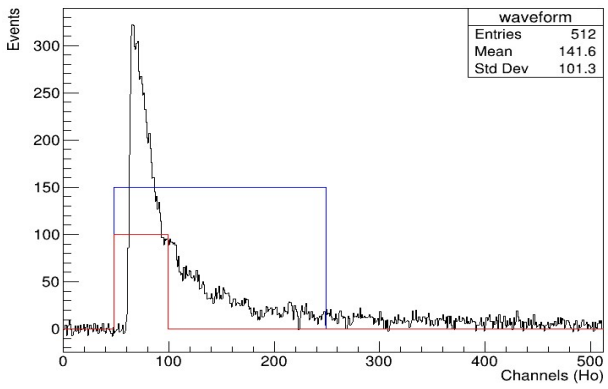

FIGURE 4.1: Q_{long} (blue) and Q_{short} (red) windows for Red Pitaya digitizer.

way that they allow to obtain the best values of energy resolution and peak efficiency. To

achieve the mentioned objective, a source of ^{137}Cs and ^{252}Cf were used with both digitizers (CAEN and Red Pitaya) in the experimental setting shown in figure 4.2.

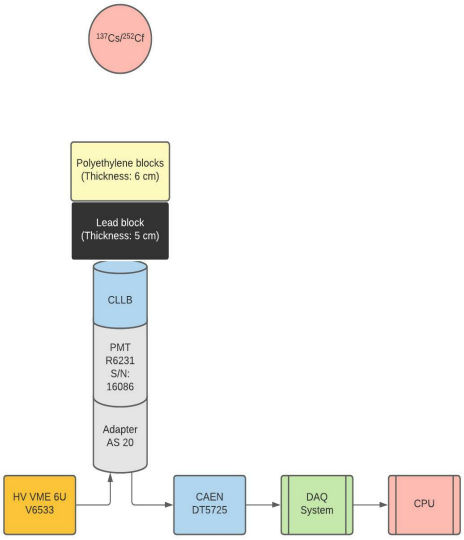

FIGURE 4.2: Experimental setup for determining optimal Q_{long} and Q_{short}.

For the optimization of the Q_{long} parameter, the ^{137}Cs source was set at 10 cm from the CLLB detector with each digitizer separately. During this stage, the value of the Q_{short} parameter was set approximately at the 25% of the value of the Q_{long} parameter since from prior measurements this was a reference value to start with. It's important to note that in this case no lead or polyethylene blocks were set between the source and the detector as it's indicated in the figure 4.2. Once obtained the spectrum of this source (figure 4.3), and with the aid of the fit tool of the ROOT software interface, the sigma and mean position of the 0.662 MeV characteristic gamma emission peak were obtained in order to calculate the resolution through the equation 4.1 [7]:

$$R = \frac{\text{FWHM}}{\text{H}_0} \tag{4.1}$$

where FWHM$= 2.35\sigma$, and H_0 is the average pulse height.

These relations and equation 4.1 itself can be used because the shape of the gamma peak of the ^{137}Cs (and the other sources mentioned) can be approximated as a Gaussian distribution [7]. It is important to mention that in the case of the CAEN digitizer, the spectrum is the same with the difference that the channel axis cover a wider range, and the amplitude of the peak is almost twice the amplitude of the peak shown in figure 4.3 corresponding to the Red Pitaya digitizer. This is due to the digital conversion rate of the digitizers; as it can be reviewed in table 2.2, Red Pitaya has half the value respect to CAEN.

The procedure consisted in calculating the resolution of a given value of the Q_{long} parameter. This value was changed until obtain the minimum value of FWHM, which in turn would give the best resolution. The different values of Q_{long} for the Red Pitaya digitizer with their respective resolution values are shown in table 4.1. In this, it can be seen that the best resolution is achieved at a Q_{long} of 200 ns.

In the case of the CAEN digitizer, the optimal Q_{long} value was achieved at 450 ns as it's shown in the table 4.2. A relevant detail to remark is that in both digitizers the differences in resolution weren't too evident. The resolution is very similar for all the Q_{long}s selected. The difference between these quantities is slightly evident in the Red Pitaya digitizer; the

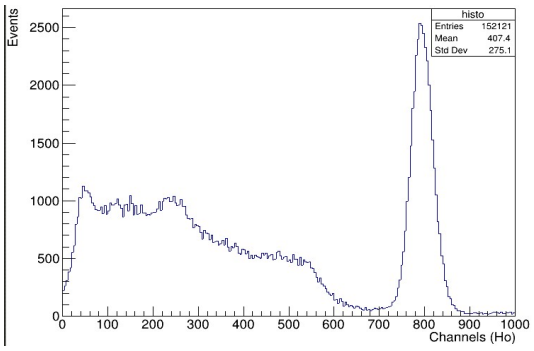

FIGURE 4.3: ^{137}Cs spectrum for the Red Pitaya digitizer.

Q_{long} (ns)	H_0	error (H_0)	σ	error (σ)	R (%)
260	837.19	0.157	29.65	0.132	8.323
250	830.97	0.160	28.17	0.147	7.967
240	824.58	0.154	27.39	0.139	7.805
220	810.68	0.144	25.87	0.128	7.499
210	802.93	0.141	25.04	0.129	7.329
200	786.22	0.131	23.70	0.116	7.084
190	794.94	0.136	24.38	0.123	7.207
180	795.62	0.126	24.22	0.124	7.154
170	802.15	0.125	25.13	0.126	7.362
150	809.58	0.123	26.06	0.130	7.565
120	816.23	0.145	26.12	0.132	7.520
100	832.45	0.149	27.05	0.146	7.636

TABLE 4.1: Red Pitaya Q_{long} optimization.

range of resolution is between 7.084% and 8.323% whereas in the CAEN digitizer is between 4.766% and 4.961%.

Q_{long} (ns)	H_0	error (H_0)	σ	error (σ)	R (%)
340	49272.2	6.994	1022.52	8.828	4.877
345	49432.1	7.315	1043.47	9.359	4.961
350	49609.8	6.676	1032.94	7.938	4.893
360	49889.5	7.552	1022.18	10.285	4.815
400	51036.5	6.908	1051.12	8.291	4.840
420	51525.3	6.977	1056.78	8.431	4.820
430	51758.8	7.042	1062.02	8.532	4.822
440	51987.4	6.682	1059.8	7.551	4.791
450	52191.1	7.504	1058.28	9.732	4.766
460	52420.9	6.785	1073.58	7.805	4.813
470	52656.2	6.263	1108.38	6.441	4.947
500	53237.9	5.974	1108.64	5.528	4.894
510	53418.5	6.029	1119.6	5.686	4.925
520	53564.5	6.529	1110.77	6.977	4.873

TABLE 4.2: CAEN Q_{long} optimization.

The Q_{long} vales of both digitizers were plotted versus the resolution (figure 4.4) in order to have a graphical view of the optimization procedure and the optimal values obtained

during it. Despite the values are very similar between them as it was mentioned, in the plots is more evident that there is in fact a minimum value of Q_{long}.

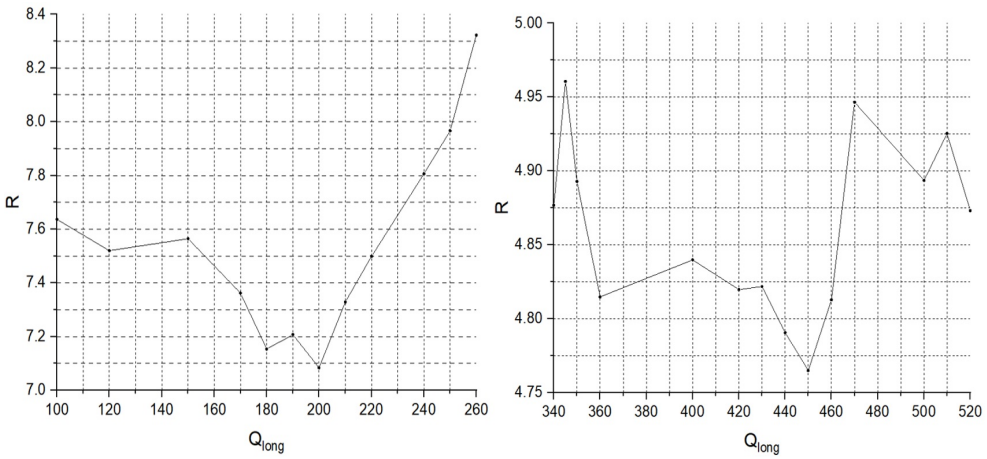

FIGURE 4.4: Resolution vs Q_{long} of Red Pitaya (left) and CAEN (right) digitizers.

For the calculation of Q_{short}, the procedure and experimental setup were very similar to the ones used for Q_{long}. In this case, a 5 cm thick lead block together with a set of three blocks of polyethylene with a total thickness of 6 cm were set just in front of the CLLB detector. The source in this case was ^{252}Cf. This setup can be appreciated in figure 4.5, and is important to remark the detail that in this case the source was set just next to the lead block and not with a distance in between like in the mentioned figure.

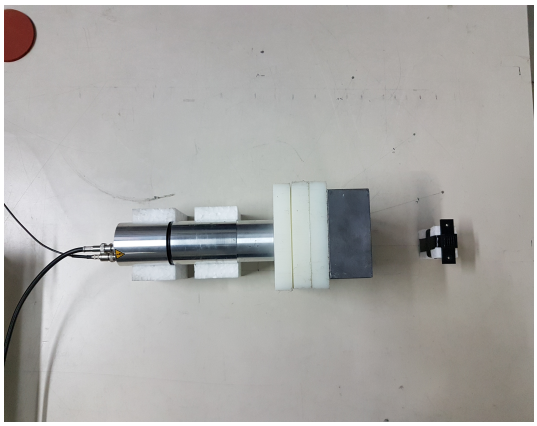

FIGURE 4.5: Experimental setup for the calculation of Q_{short}.

In this case, the Figure of Merit (FoM) was used instead of the resolution. FoM is an important parameter in the application of the PSD techniques. It's defined as the measurement of the discrimination capacity of the system (scintillator coupled with the pulse processing electronics) of many type of events, in the current case neutrons and gamma photons, in a specific application [10]. When a PSD technique is applied, the measurement is expressed through a PSD parameter histogram in which it's possible to identify the distributions that corresponds to each specific event involved in the detection process. For instance, in the current scenario, the figure 4.6 shows the histogram of a PSD parameter which contains the Gaussian distributions corresponding to the gamma photons at the left, and the neutrons at the right. The histogram of the CAEN digitizer is similar but with different H_0 positions and amplitudes for the gamma and neutron distributions (in this case H_0 is X_γ for the gamma distribution and X_n for the neutrons one).

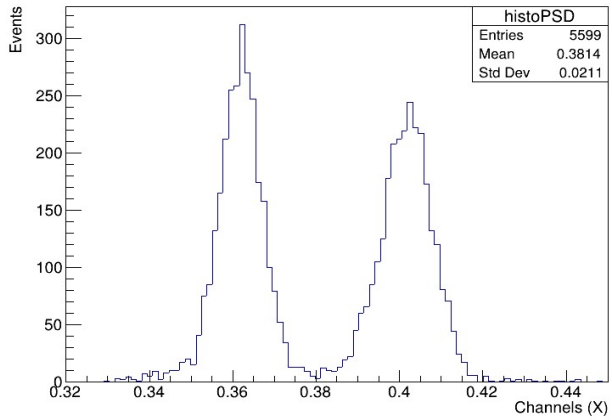

FIGURE 4.6: Histogram of the PSD parameter of the Red Pitaya digitizer. Gamma photons distribution (left), neutrons distribution (right).

As in the previous calculations with Q_{long}, many values of Q_{short} were tested to obtain the optimal FoM through the equation:

$$\text{FoM} = \frac{X_n - X_\gamma}{(\sigma_\gamma + \sigma_n)2.35} \tag{4.2}$$

The denominator of the function represents the sum of FWHM of both neutrons and gamma photons distributions. Again, the different selected Q_{short} values and their corresponding FoM for both digitizers are shown in tables 4.3 and 4.4. Here it can be observed that for the Red Pitaya digitizer the optimal Q_{short} value is 50 ns since with this, the value of the FoM is maximum. For the the CAEN digitizer the optimal Q_{short} is 105 ns.

Q_{short} (ns)	X_γ	X_n	σ_γ	σ_n	FoM
40	0.457	0.495	0.007	0.007	1.155
45	0.404	0.444	0.006	0.007	1.309
50	0.324	0.365	0.006	0.006	1.454
55	0.361	0.401	0.006	0.006	1.418
60	0.293	0.332	0.006	0.006	1.383
65	0.265	0.303	0.0055	0.006	1.406

TABLE 4.3: Red Pitaya Q_{short} optimization

Q_{short} (ns)	X_γ	X_n	σ_γ	σ_n	FoM
120	0.317	0.356	0.005	0.005	1.660
110	0.351	0.393	0.005	0.005	1.787
105	0.368	0.411	0.005	0.005	1.830
100	0.388	0.429	0.005	0.005	1.745
90	0.434	0.476	0.006	0.006	1.489
80	0.492	0.531	0.006	0.006	1.383
150	0.239	0.277	0.005	0.005	1.617

TABLE 4.4: CAEN Q_{short} optimization

The behavior the FoM values obtained, turned to be clearer compared with the resolution values of the Q_{long} calculations. That is, the differences between the FoM values of

each corresponding Q_{short} are more evident between them, and there is a clear decreasing tendency around the maximum FoM value. This can be seen easier in the plots of figure4.7.

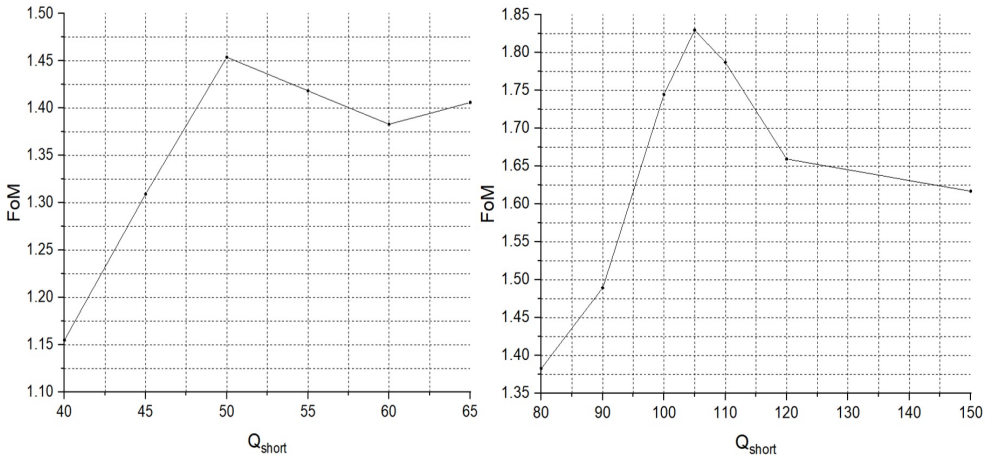

FIGURE 4.7: FoM vs Q_{short} of Red Pitaya (left) and CAEN (right) digitizers.

4.2 Angular Efficiency

This set of experiments had the objective to show the detection homogeneity of the CLLB detector. To accomplish this purpose, different gamma sources (^{133}Ba, ^{60}Co, ^{22}Na, and ^{137}Cs) were set at a fixed distance of 29.5 cm from the geometrical center of the detector. Then, each one of the sources was changing position along a circumference with this center. The experimental setting is shown in figure 4.8. The angles measured were of 0°, 8°, 28.7°, 56.5°, and 90°. The digitizer used in these tests was the CAEN since the priority of them is to show the homogeneity of the detector.

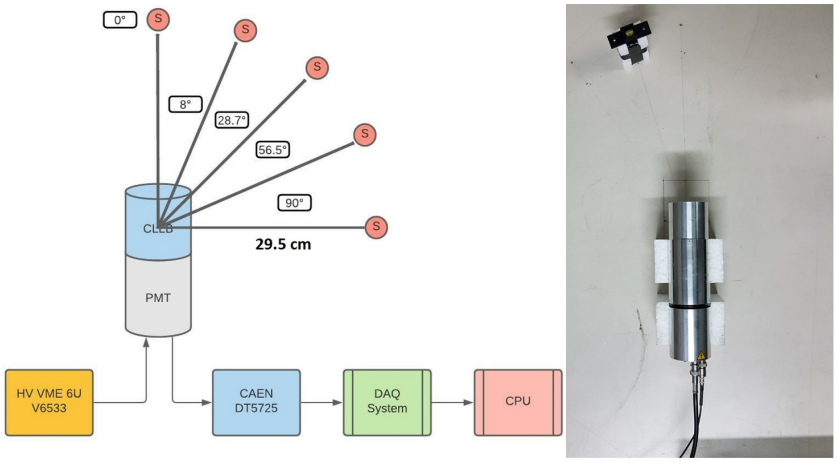

FIGURE 4.8: Experimental setup for the efficiency calculation changing the position of the source (angle).

In addition, Monte Carlo simulations were performed previously in order to have a clearer idea about what would be the response of the detector to the gamma radiation of the sources. In these simulations, the specific experimental conditions of each test were configured: type of radiation emitted (gamma rays), type of source (isotropic), shape of the source (point-like), position, energy of the emitted gamma rays (this depended on which of the four sources was employed), characteristic gamma peak or peaks depending on the

source, intensity, and number of particles to be simulated, which in these cases was of 4×10^7 events. The figure 4.9 represents how these simulations look like. As it can be appreciated, the point-like source emits radiation towards the front base of the cylinder (CLLB detector) just like in the real experimental setup.

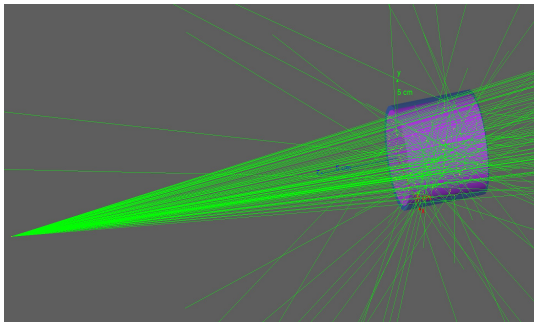

FIGURE 4.9: Experimental setup visualized in GEANT4.

The efficiency considered in the simulations was the absolute efficiency (ϵ_{abs}) of the detector, which is defined as the number of pulses recorded by the CLLB, divided by the number of radiation quanta emitted by the source [7]:

$$\epsilon_{abs} = \frac{\text{No. of pulses recorded}}{\text{number of radiation quanta emitted by the source}} \tag{4.3}$$

It's worth mentioning that the intrinsic efficiency (ϵ_{int}) is defined as the number of pulses recorded, divided by the number of radiation quanta incident on the CLLB [7]:

$$\epsilon_{int} = \frac{\text{No. of pulses recorded}}{\text{number of radiation quanta incident on the detector}} \tag{4.4}$$

The relation between both efficiencies is then given by:

$$\epsilon_{int} = \epsilon_{abs} \frac{4\pi}{\Omega} \tag{4.5}$$

where Ω is the solid angle of the detector seen from the current position of the source. The reason of using the absolute instead of the intrinsic efficiency is because the equation 4.5 can be used only when the plane of the detector surface is parallel to the plane of the source. Since there is an angle variation between the source and the frontal surface of the detector, the equation would be more difficult to apply.

An important detail to mention is that the efficiency calculation that was made, is actually the peak efficiency since the region of the spectra considered in the analysis of the experimental tests and simulations was only the characteristic gamma peak (or peaks if there were more than one) and not the whole spectrum.

The procedure to calculate the efficiency in the simulations was to divide the registered number of events of the specific conditions mentioned (type of particles, energy, intensity), by the total number of the events generated in the simulation. This last number is actually multiplied by the specific intensity of the gamma peaks of each different source. For instance, if a ^{137}Cs spectrum was analyzed, the total number of events (4×10^7) was multiplied by the intensity of the 0.662 MeV characteristic gamma peak (0.85) [13]. If there were more than one gamma peak like in the ^{133}Ba source, the peak intensities took the largest intensity as the reference, and then proceed with the same calculation for each one of the peaks.

4.2.1 Simulations results

The results obtained from the simulations are shown from tables 4.5 to 4.9. For each source there were five measurements corresponding to the five different angles used. The error taken into account was obtained with the relation $\sqrt{N}/N$, where N is the number of events of each specific energy indicated in the sources for the gamma peaks observed in the spectra. The angle is given in degrees and the energy in MeV indicated inside the parenthesis corresponds to the main gamma peaks of each radioactive source.

(°)	Evts. (0.662 MeV)	ϵ_{abs}	Error (%)
0	4330	0.069	0.015
8	4410	0.070	0.015
28.7	4443	0.071	0.015
56.5	4678	0.075	0.015
90	5189	0.083	0.014

TABLE 4.5: ^{137}Cs gamma photons simulation.

(°)	Evts. (1.17MeV)	ϵ_{abs}	Error (%)	Evts. (1.33MeV)	ϵ_{abs}	Error (%)
0	7883	0.039	0.011	6744	0.034	0.012
8	7917	0.040	0.011	6753	0.034	0.012
28.7	8014	0.040	0.011	6980	0.035	0.012
56.5	8689	0.043	0.011	7266	0.036	0.012
90	7984	0.040	0.011	6674	0.033	0.012

TABLE 4.6: ^{60}Co gamma photons simulation.

(°)	Evts. (0.511MeV)	ϵ_{abs}	Error (%)	Evts. (1.274 MeV)	ϵ_{abs}	Error (%)
0	23105	0.090	0.007	5218	0.037	0.014
8	23191	0.090	0.007	5071	0.035	0.014
28.7	23615	0.092	0.007	5137	0.036	0.014
56.5	25501	0.099	0.006	5548	0.039	0.013
90	28011	0.109	0.006	6180	0.043	0.013

TABLE 4.7: ^{22}Na gamma photons simulation.

(°)	Evts. (0.081MeV)	ϵ_{abs}	Error (%)	Evts. (0.2764 MeV)	ϵ_{abs}	Error (%)
0	24424	0.224	0.006	4093	0.172	0.016
8	24156	0.221	0.006	3996	0.168	0.016
28.7	27000	0.247	0.006	4368	0.184	0.015
56.5	30760	0.282	0.006	4806	0.202	0.014
90	29445	0.270	0.006	5252	0.221	0.014

TABLE 4.8: ^{133}Ba gamma photons simulation (1).

4.2.2 Experimental results

Before making the experimental tests, a calibration of the digitizer with the main gamma peaks of the different sources was performed. The calibration curve is presented in the figure 4.10.

(°)	Evts. (0.3028MeV)	ϵ_{abs}	Error (%)	Evts. (0.356 MeV)	ϵ_{abs}	Error (%)
0	9063	0.149	0.011	26337	0.128	0.006
8	9066	0.149	0.011	26281	0.128	0.006
28.7	9678	0.159	0.010	27331	0.133	0.006
56.5	10593	0.174	0.010	29352	0.142	0.006
90	11225	0.184	0.009	32069	0.156	0.006

TABLE 4.9: ^{133}Ba gamma photons simulation (2).

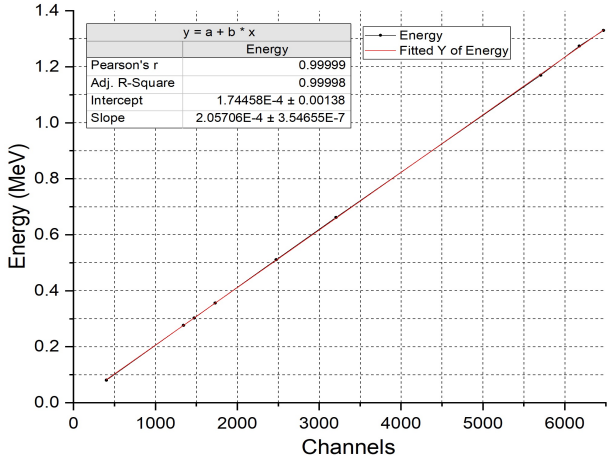

FIGURE 4.10: Energy calibration of CAEN digitizer.

To obtain the peak efficiency in the experimental tests, the equation used was:

$$\epsilon_{\text{peak}} = \frac{A}{N/\Delta t} \tag{4.6}$$

where A is the area under the gamma peak analyzed, and $N/\Delta t = \gamma A(t)$. At the same time, γ is the intensity of the particular gamma peak [13] and $A(t)$ is the activity of the source employed. In order to calculate the mentioned area, the fityk software was used. As it's shown in the figure 4.11, this program allows to visualize the spectrum, select a particular region, in this case the gamma peaks of interest, and then make a set of fits (Gaussian, linear, etc.) to finally obtain different parameters like the area, FWHM, mean value of the selected peak, and its height.

The spectra obtained correspond to the CAEN digitizer as it was mentioned at the beginning of this section. In the figure 4.12, are shown the spectra of the four different gamma sources employed in these experimental tests. The red spectra corresponds to a background measured during several hours without any of the sources present in the surroundings of the CLLB detector. The blue spectra represent the original gamma sources measurements, and the black spectra are the difference between the blue and the red ones; by this way, black spectra represent the gamma sources measurements without background noise. These spectra were the ones analyzed in the software fityk to obtain the area under the gamma peaks and the other parameters mentioned.

From the tables 4.10 to 4.13 are the experimental peak efficiencies of each of the tested sources at the five different angles. In the third column, it was necessary to make a simple conversion between the units used in the fityk software and the bins used in the root macro. The area (A) is divided by the number of bins corresponding to one length unit (from point to point of the spectra shown in figure 4.11) of the program. The energy (MeV) inside the parenthesis indicates the specific peak of the spectra as is also indicated in the tables with the

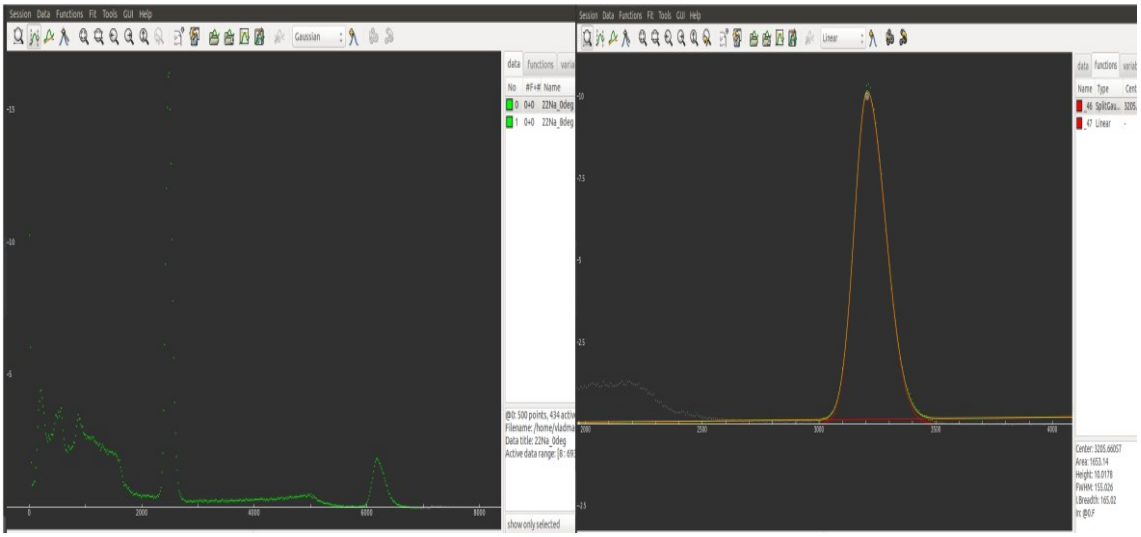

FIGURE 4.11: Calculation of the area under the gamma peak with Fityk software.

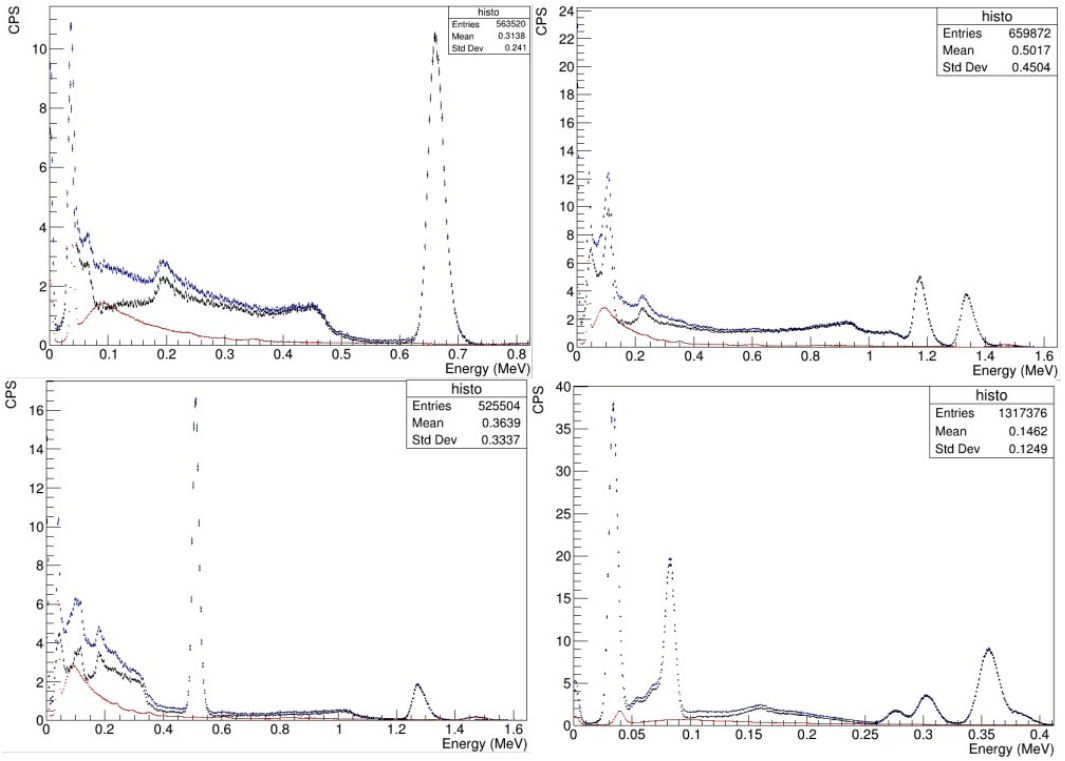

FIGURE 4.12: Spectra obtained from the gamma sources with CAEN digitizer at 0°. ^{137}Cs (top left); ^{60}Co (top right); ^{22}Na (bottom left); and ^{133}Ba (bottom right).

results of the simulations (tables 4.5 to 4.9). The intensities (γ) of each source were obtained from [13]. The calculated activities ($A(t)$) of each source were 337.255 kBq (^{137}Cs), 176.682 kBq (^{60}Co), 80.118 kBq (^{22}Na), and 275.003 kBq (^{133}Ba). The time indicated in the source container was from June 15th 2015.

(°)	$(MeV)_{peak}$	A/bin	H_0	FWHM	ϵ_p
0	0.662	206.643	3205.661	155.026	0.072
8	0.662	196.739	3202.935	155.053	0.069
28.7	0.662	208.821	3177.066	156.681	0.073
56.5	0.662	211.771	3182.858	161.475	0.074
90	0.662	214.046	3187.087	163.645	0.075

TABLE 4.10: Experimental efficiencies ϵ_p for the gamma peak of ^{137}Cs source.

(°)	$(MeV)_{peak}$	A/bin	H_0	FWHM	ϵ_p(1.17)	ϵ_p (1.33)
0	1.17	69.929	5704.060	235.854	0.040	-
0	1.33	63.474	6472.405	268.643	-	0.036
8	1.17	72.252	5692.528	245.925	0.041	-
8	1.33	61.928	6465.612	266.657	-	0.035
28.7	1.17	68.764	5650.157	232.355	0.039	-
28.7	1.33	63.254	6415.364	263.374	-	0.036
56.5	1.17	69.554	5652.244	244.725	0.039	-
56.5	1.33	62.641	6424.949	272.990	-	0.035
90	1.17	70.124	5661.896	249.161	0.040	-
90	1.33	65.703	6431.251	284.961	-	0.037

TABLE 4.11: Experimental efficiencies ϵ_p for the gamma peaks of ^{60}Co source.

(°)	$(MeV)_{peak}$	A/bin	H_0	FWHM	ϵ_p (0.511)	ϵ_p (1.274)
0	0.511	137.034	2474.762	130.390	0.095	-
0	1.274	29.535	6177.024	255.669	-	0.037
8	0.511	134.521	2472.852	130.495	0.093	-
8	1.274	28.489	6172.958	249.810	-	0.036
28.7	0.511	138.063	2454.241	131.008	0.096	-
28.7	1.274	29.551	6125.340	259.103	-	0.037
56.5	0.511	142.236	2459.385	136.138	0.099	-
56.5	1.274	29.759	6134.583	266.838	-	0.037
90	0.511	143.814	2463.335	138.946	0.100	-
90	1.274	30.381	6137.375	266.714	-	0.038

TABLE 4.12: Experimental efficiencies ϵ_p for the gamma peaks of ^{22}Na source.

4.2.3 Simulations vs experimental results

From the tables 4.14 to 4.18 are shown the comparisons between the efficiencies obtained with the Monte Carlo (MC) simulations (ϵ_{abs}), and the peak efficiencies obtained experimentally (ϵ_p) expressed in percentages. Right after the table of each source, are also presented the plots (figure 4.13 to 4.16) of the experimental results and simulations with the purpose of having a better visualization of both behaviors. For the ^{137}Cs and ^{60}Co sources, the difference of both efficiencies at any given angle was less than 10%, which indicates that there is a very good match between the experiments and the simulations. For the case of the ^{22}Na source, the difference between both efficiencies was also less than 10% except in the 90° angle, which yielded a difference of 12.165% for the 1.274 MeV peak. Nevertheless, the match between the experimental results and simulations was also in a very good range.

In the case of the ^{133}Ba source, the behavior had significant variations depending on the peak analyzed. In the 0.081 MeV peak the difference between the efficiencies kept a similar

(°)	$(MeV)_{peak}$	A/bin	H_0	FWHM	$\epsilon_p(0.081)$	$\epsilon_p(0.2764)$	$\epsilon_p(0.3028)$	$\epsilon_p(0.356)$
0	0.081	200.420	402.202	45.23	0.214	-	-	-
0	0.2764	29.279	1342.709	74.82	-	0.149	-	-
0	0.3028	77.731	1472.689	89.64	-	-	0.154	-
0	0.356	216.813	1729.791	93.33	-	-	-	0.127
8	0.081	207.313	402.333	45.53	0.221	-	-	-
8	0.2764	29.109	1342.761	74.67	-	0.148	-	-
8	0.3028	77.563	1472.688	89.52	-	-	0.154	-
8	0.356	216.624	1729.773	93.27	-	-	-	0.127
28.7	0.081	243.544	400.546	47.14	0.260	-	-	-
28.7	0.2764	28.706	1342.879	74.27	-	0.146	-	-
28.7	0.3028	77.183	1472.684	89.27	-	-	0.153	-
28.7	0.356	216.173	1729.727	93.14	-	-	-	0.127
56.5	0.081	241.848	402.800	46.65	0.258	-	-	-
56.5	0.2764	28.422	1342.959	74.02	-	0.144	-	-
56.5	0.3028	76.896	1472.684	89.08	-	-	0.153	-
56.5	0.356	215.831	1729.692	93.04	-	-	-	0.126
90	0.081	223.003	403.628	47.19	0.238	-	-	-
90	0.2764	28.422	1342.959	74.02	-	0.144	-	-
90	0.3028	76.896	1472.684	89.08	-	-	0.153	-
90	0.356	215.831	1729.692	93.04	-	-	-	0.126

TABLE 4.13: Experimental efficiencies ϵ_p for the gamma peaks of ^{133}Ba source.

(°)	ϵ_{abs}	ϵ_p	Diff. (%)
0	0.069	0.072	4.167
8	0.070	0.069	1.429
28.7	0.071	0.073	2.740
56.5	0.075	0.074	1.333
90	0.083	0.075	9.639

TABLE 4.14: Difference between simulation and experimental results for ^{137}Cs source.

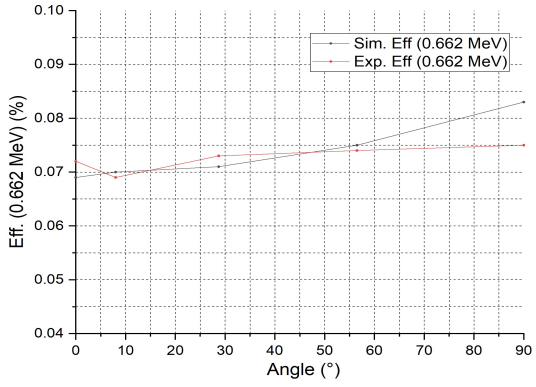

FIGURE 4.13: Experimental results (red) vs simulation (blue) for ^{137}Cs.

tendency respect the previous sources; only the measurement at the 90° angle the difference was slightly larger than 10% (11.693%). In contrast, the 0.2764 MeV peak showed the largest discrepancies between experiment and simulation among all the other gamma peaks since

(°)	ϵ_{abs} (1.17 MeV)	ϵ_p (1.17 MeV)	Diff.(%)	ϵ_{abs} (1.33 MeV)	ϵ_p (1.33 MeV)	Diff.(%)
0	0.039	0.040	1.398	0.034	0.036	6.394
8	0.040	0.041	3.388	0.034	0.035	3.591
28.7	0.040	0.039	2.734	0.035	0.036	3.119
56.5	0.043	0.039	10.290	0.036	0.035	3.598
90	0.040	0.040	0.135	0.033	0.037	9.869

TABLE 4.15: Difference between simulation and experimental results for ^{60}Co source.

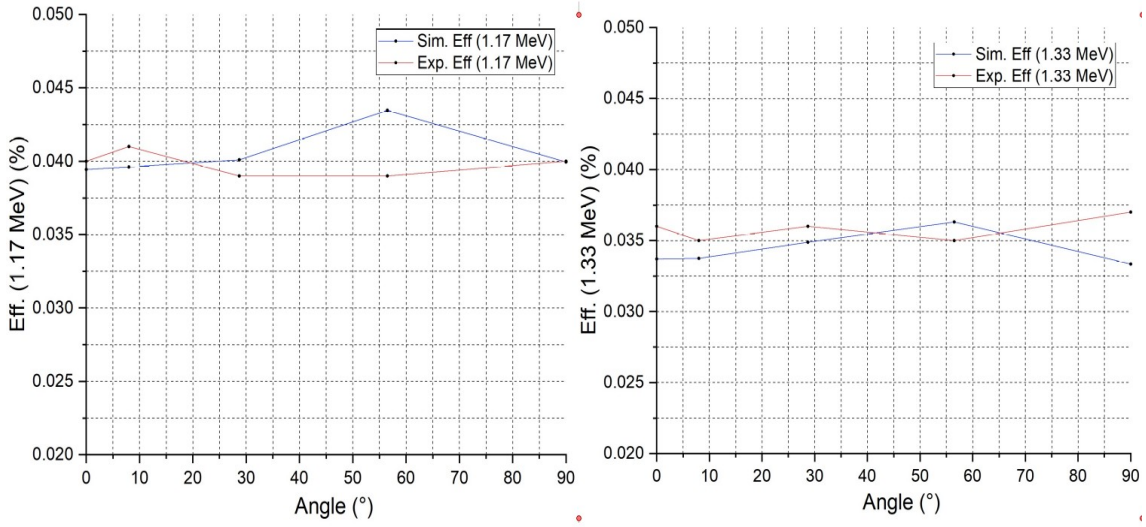

FIGURE 4.14: Experimental results (red) vs simulation (blue) for ^{60}Co.

(°)	ϵ_{abs} (0.511 MeV)	ϵ_p (0.511 MeV)	Diff.(%)	ϵ_{abs} (1.274 MeV)	ϵ_p (1.274 MeV)	Diff.(%)
0	0.090	0.095	5.422	0.037	0.037	1.275
8	0.090	0.093	3.028	0.035	0.036	1.391
28.7	0.092	0.096	4.341	0.036	0.037	2.807
56.5	0.099	0.099	0.168	0.039	0.037	4.734
90	0.109	0.100	8.196	0.043	0.038	12.165

TABLE 4.16: Difference between simulation and experimental results for ^{22}Na source.

(°)	ϵ_{abs} (0.081 MeV)	ϵ_p (0.081 MeV)	Diff.(%)	ϵ_{abs} (0.2764 MeV)	ϵ_p (0.2764 MeV)	Diff.(%)
0	0.224	0.214	4.275	0.172	0.149	13.435
8	0.221	0.221	0.047	0.168	0.148	11.929
28.7	0.247	0.260	4.948	0.184	0.146	20.519
56.5	0.282	0.258	8.365	0.202	0.144	28.752
90	0.270	0.238	11.693	0.221	0.144	34.802

TABLE 4.17: Difference between simulation and experimental results for ^{133}Ba source (1).

the minimum difference in this case was of 11.929% at 8° and the largest one was of 34.802% at 90°. The explanation of these large variations in this particular peak may be found in the figure 4.12. Analyzing the ^{133}Ba spectrum, it can be appreciated that the 0.2764 MeV peak is pretty close to the next peak. Besides, its not-well defined shape made difficult the analysis

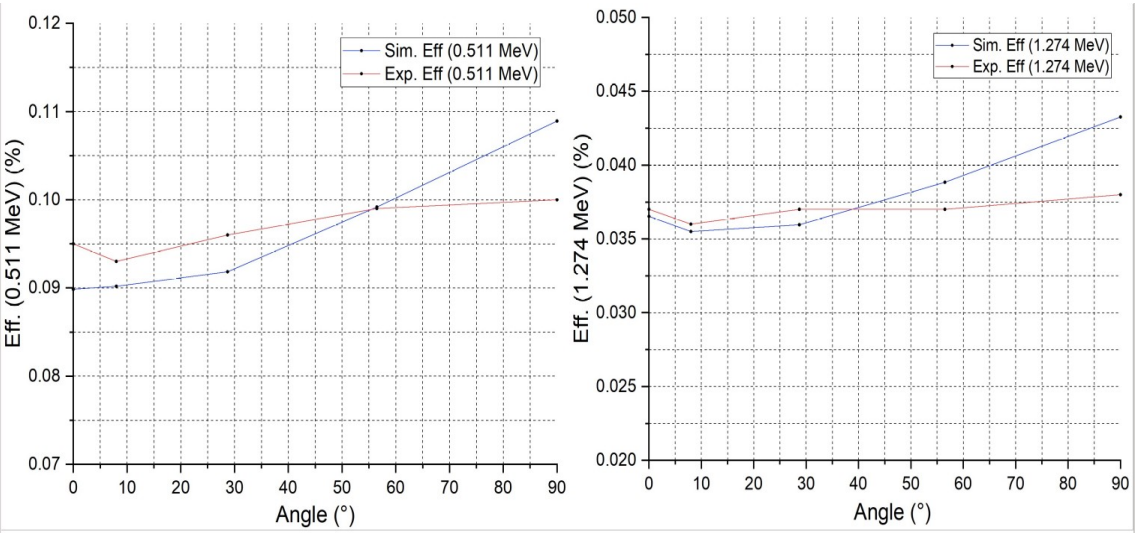

FIGURE 4.15: Experimental results (red) vs simulation (blue) for ^{22}Na.

(°)	ϵ_{abs} (0.3028 MeV)	ϵ_p (0.3028 MeV)	Diff.(%)	ϵ_{abs} (0.356 MeV)	ϵ_p (0.356 MeV)	Diff.(%)
0	0.149	0.154	3.382	0.128	0.127	0.636
8	0.149	0.154	3.350	0.128	0.127	0.425
28.7	0.159	0.153	3.706	0.133	0.127	4.250
56.5	0.174	0.153	12.024	0.142	0.126	11.545
90	0.184	0.153	16.977	0.156	0.126	19.039

TABLE 4.18: Difference between simulation and experimental results for ^{133}Ba source (2).

with the fityk software since the fit developed didn't covered the peak with precision.

The last two peaks of the ^{133}Ba source (0.3028 MeV and 0.356 MeV) presented a similar behavior. Both of them had an efficiency difference larger than 10% at the 56.5° and 90° angles. In the rest of the angles the difference was of less than 10%. For the 0.3028 MeV peak, the proximity to the 0.02764 MeV peak could also represent a relevant cause of these variations, as it was explained for the previous case, whereas in the last peak (0.356 MeV), the largest difference was at the 90° measurement, and it was significantly larger than the rest of the values of this peak (19.039% vs the second largest value (11.545%).

Finally, but not less important, another parameter that must be observed in the tables of the experimental results (4.10 to 4.13) is the H_0 parameter that indicates the position of the average pulse height. Even with the angle variations, the peak positions of each source remained almost in the same position. In fact, the difference between the five angle measurements for each one of the gamma peaks present on each source was less than 1% in all the cases, so it can be said that they remained practically in the same position through all the experimental tests.

4.3 Energy calibration, resolution, and linearity

As it was indicated at the beginning of this chapter, the Red Pitaya digitizer is the one that will be on board the UAV along with the CLLB detector. Therefore, it was necessary to perform an energy calibration with the ^{133}Ba, ^{60}Co, ^{22}Na, and ^{137}Cs gamma sources. The experimental setup was the same that the one configured to obtain the optimal Q_{long} and

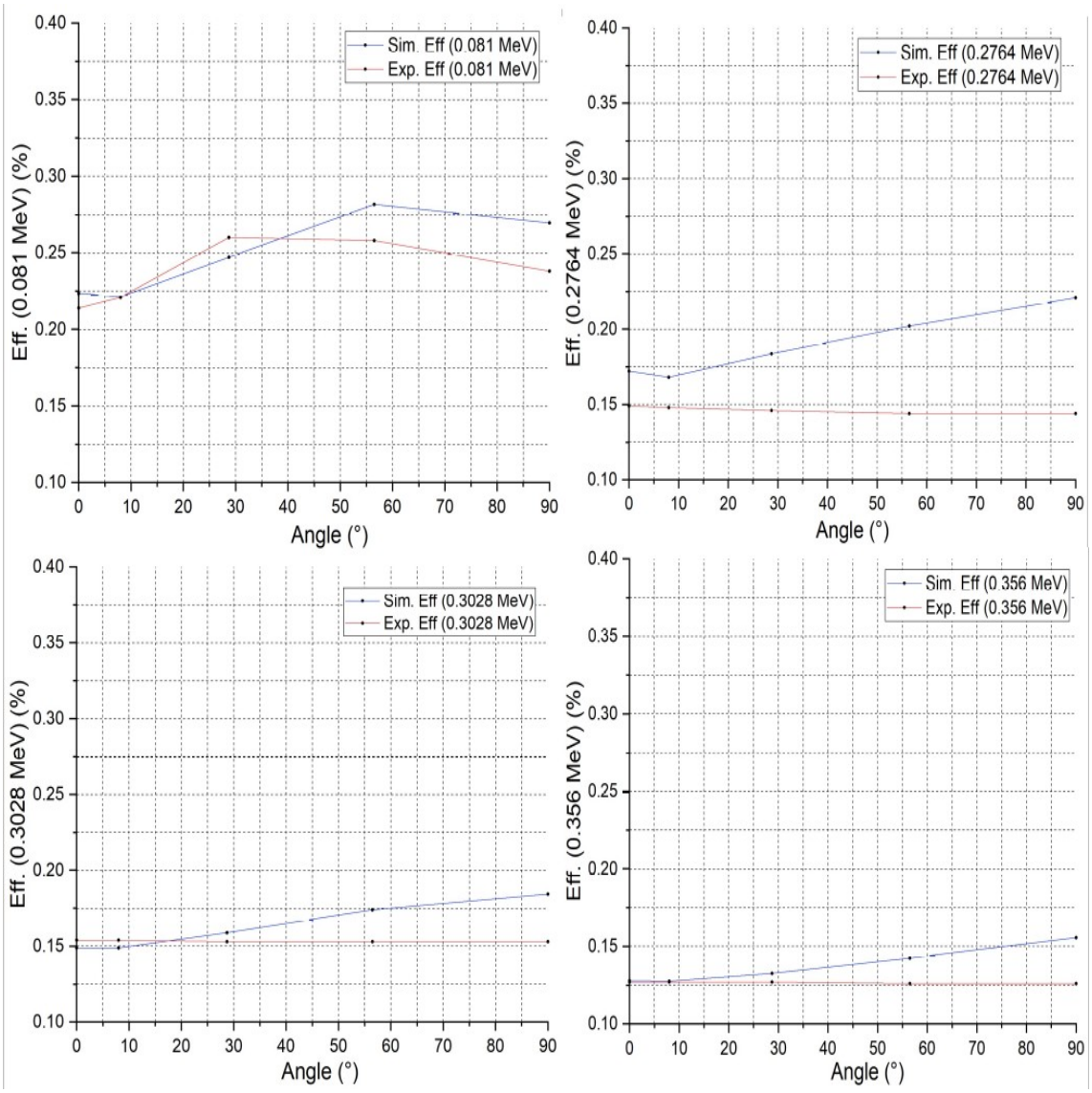

FIGURE 4.16: Experimental results (red) vs simulation (blue) for ^{133}Ba.

Q_{short} integration windows (figure 4.2 without any lead or polyethylene blocks). The difference lies in the fact that this time the additional gamma sources were employed.

Once the energy calibration was successfully performed (figure 4.17), it was possible to obtain the peak efficiency and resolution of each one of the sources; these values appear on the table 4.19. In order to calculate the efficiency and resolution, the software fityk was also employed in this section to obtain the area (A), H_0, and FHWM.

The first column of the table shows the source used and the specific gamma peak analyzed, which is indicated inside the parenthesis with its energy in MeV. Like the same way that in the previous section, in the second column the area was divided by the bins used in the root macro. One important aspect to analyze in this table is the resolution value of the ^{137}Cs source (5.303%). This resolution was even better than the one obtained in the optimization of the Q_{long} that is shown in the table 4.1, which also was made with a ^{137}Cs source. This is because at the moment of the optimization of the Q_{long} parameter for both digitizers, the Q_{short} wasn't exactly at its optimal value. In this experiment, both parameters were already optimized so the resolutions obtained were better.

The spectra obtained after the calibration can be appreciated in the figure 4.18. As in the

Source P. (MeV)	A/bin	H_0	FWHM	$A(t)$ (kBq)	ϵ_p	R (%)
^{137}Cs (0.662)	272.790	1597.704	84.721	337.255	0.095	5.303
^{22}Na (0.511)	349.638	1240.226	71.181	80.118	0.243	5.739
^{22}Na (1.274)	77.086	3088.770	136.006	80.118	0.096	4.403
^{60}Co (1.17)	172.180	2858.839	122.621	176.682	0.098	4.289
^{60}Co (1.33)	156.789	3246.874	139.268	176.682	0.089	4.289
^{133}Ba (0.081)	339.163	205.114	38.942	275.003	0.362	18.986
^{133}Ba (0.2764)	42.083	668.716	53.487	275.003	0.214	7.998
^{133}Ba (0.3028)	79.618	741.125	45.551	275.003	0.158	6.146
^{133}Ba (0.356)	312.105	863.794	61.251	275.003	0.183	7.091

TABLE 4.19: Values of resolution and peak efficiency for the Red Pitaya digitizer

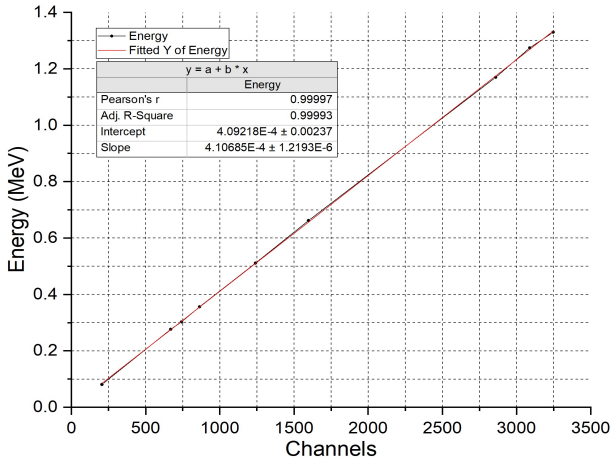

FIGURE 4.17: Energy calibration of Red Pitaya digitizer.

case of the CAEN digitizer, the background was subtracted from each of the sources. In these measurements, there wasn't angle variation; every source was set just in front of the detector in the same way that was made for 0° in the previous tests. Comparing the spectra obtained with the Red Pitaya digitizer with the ones obtained with the CAEN digitizer (figure 4.12), it can be observed that for the ^{137}Cs and ^{133}Ba spectra the amplitudes of the gamma peaks analyzed are similar in both digitizers. However, the ^{60}Co and ^{22}Na show approximately twice the amplitude in the Red Pitaya digitizer. This could be due to a different setting of these particular sources respect to the front face of the CLLB detector.

Another important detail is the ^{133}Ba spectra in both digitizers. It can be observed that there are five and no four main gamma peaks (the four analyzed through this and the previous sections). The reason that the first peak at the left wasn't considered is because it's actually composed of more than one peak, and hence it contains more than one energy overlap [13]. This would have caused a considerable lack of precision at the time of the efficiency and energy resolution calculations. Also the proximity of the 0.2764 MeV and 0.3028 MeV peaks in these spectra can be appreciated, and as it was mentioned, it represented a difficulty to make the proper fits for the area calculations with the software fityk, which in turn caused a considerable variation between the simulations and the experimental results of the efficiency.

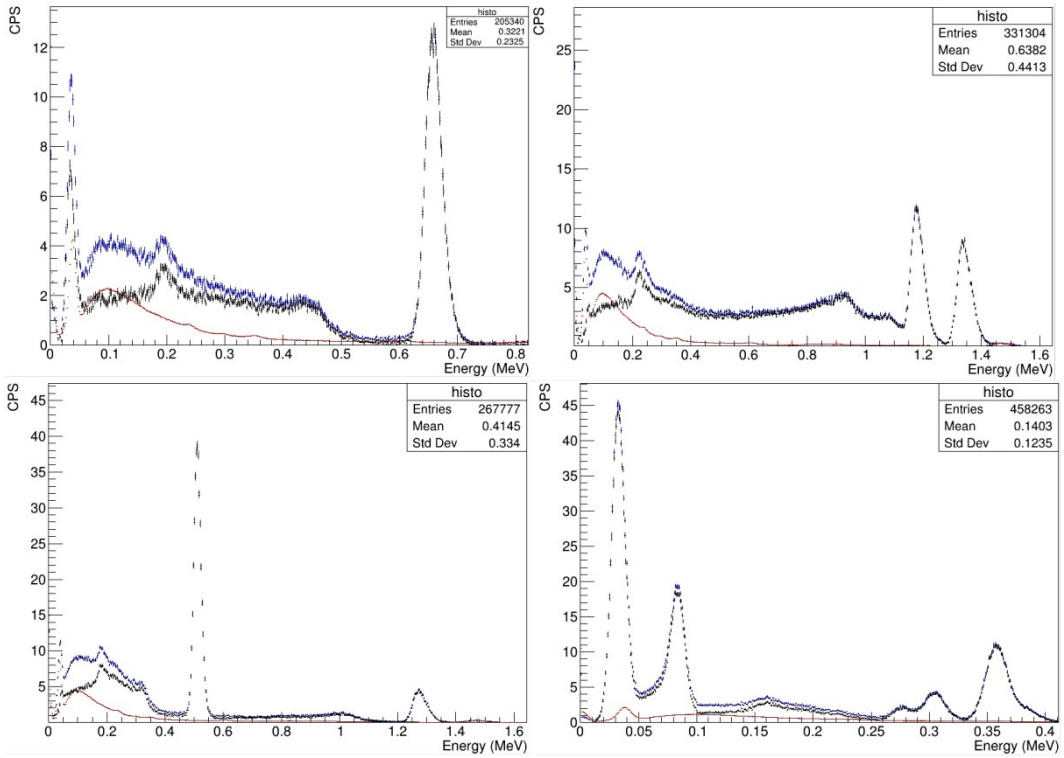

FIGURE 4.18: Spectra obtained from the gamma sources with Red Pitaya digitizer. ^{137}Cs (top left); ^{60}Co (top right); ^{22}Na (bottom left); and ^{133}Ba (bottom right).

4.4 Time Resolution

A way to suppress the characteristic internal background of some lanthanum-containing elpasolite scintillators like $LaBr_3$ or $LaCl_3$, is through time correlated measurements. Taking as basis the experimental setup depicted in figure 4.2, the CLLB detector was set in front of a EJ-228 fast plastic scintillator at a distance of 30 cm with the purpose of characterize the time resolution of the CLLB detector. Then, a ^{22}Na source was placed in the middle of the two detectors as in figure 4.19.

An off-line analysis (coincidence filter) was made on a set of digitized waveforms from both detectors to optimize the Digitial Constant Fraction Discrimination (DCFD) parameters: fraction and delay. For the optimization, three fraction values were taken into account (25%, 50%, and 75%), while the delay was varied from 40 ns to 360 ns. The best time resolution was obtained using a fraction of 25%, and a delay of 140 ns. The top plot of figure 4.20 shows the results of the described test. The resulting time spectrum with a FWHM of 1.86 ns can be observed in the bottom plot of the figure 4.20. Even with the long decay time of the CLLB signals, the resulting time resolution is very similar to the one of the NaI(Tl), which is about 250 ns. For this reason, this detector is also proper for many applications in the area of homeland and nuclear safety.

4.5 High rate dead time

In this section, the high rate dead time of the Red Pitaya digitizer was calculated taking the CAEN digitizer rate as a reference. High rate tests are performed using a high gamma rate flux by moving closer to the detector, different gamma sources and the neutron one. This is an important feature to be considered for the specific objectives of the UAV. In particular,

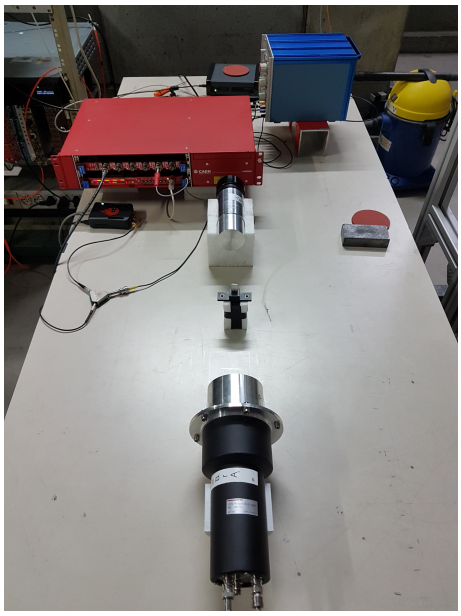

FIGURE 4.19: Experimental setup for time resolution calculation.

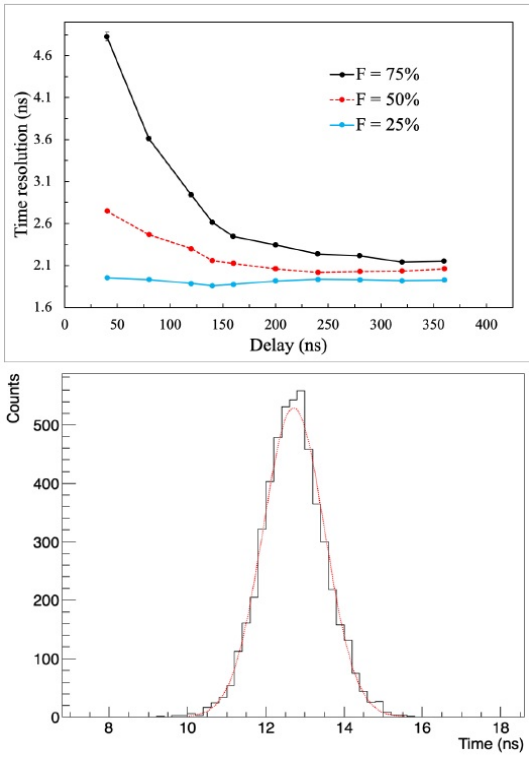

FIGURE 4.20: Time resolution for different fraction and delay values (top); time spectrum of the coincidence experiment with ^{22}Na source (bottom).

the capacity to sustain high rate and to discriminate neutrons in a high gamma rate are two important features for the security applications.

The correspondent energy calibrations with the four gamma sources (^{137}Cs, ^{60}Co, ^{22}Na, and ^{133}Ba), were performed for both digitizers. The experimental setup was the one set for the Q parameters calculation (figure 4.2, without the lead or polyethylene blocks). A prolonged measurement of about 15 minutes with the ^{60}Co source was made in both digitizers connected in parallel to the CLLB detector; meanwhile, through the ABCD (Acquisition and

Broadcast of Collected Data) interface, the rate of the CAEN digitizer was decreasing from approximately 25 kHz to 0 in intervals of about 5 kHz. The time of the measurement was arbitrary since the main objective was to have at least 10 seconds in each rate interval. The final shape of the measurement can be appreciated in the figure 4.21.

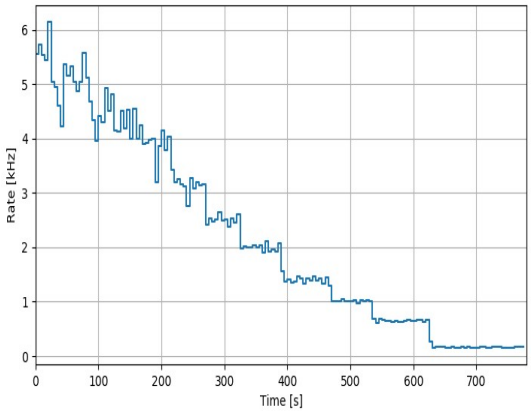

FIGURE 4.21: Red Pitaya digitizer high rate respect to CAEN digitizer.

For each one of the steps (rate intervals showed in figure 4.22), the average rate of both CAEN and Red Pitaya digitizers was calculated, as well as the rate ratio between both of them. This information is presented on table 4.20.

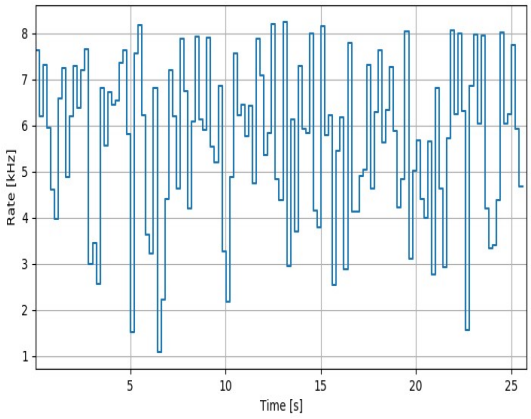

FIGURE 4.22: Interval (step) of the Red Pitaya digitizer.

From the information of the table it is possible to obtain the behavior of the rate of the Red Pitaya respect to the CAEN, which is expressed in logarithmic scale in the top plot of the figure 4.23. Also the behavior of the fraction (ratio) of the Red Pitaya respect to the CAEN rate is depicted here (bottom plot of the figure). This fraction is calculated as $1 - \frac{\text{Red Pitaya rate}}{\text{CAEN rate}}$. The uper plot of the figure includes two curves. The one in red is a $y = x$ reference curve with the CAEN average rates. The black curve represents the Red Pitaya average rates; hence, it can be seen that after 2 kHz, the rate increase in the Red Pitaya starts getting far from the rate interval increases of the CAEN. The data provided for the table and plots establishes that at rates over 20 kHz (CAEN) the Red Pitaya digitizer reaches a stability point that corresponds to almost 6 kHz.

CAEN Interv. (s)	CAEN avg. Rate (kHz)	RP avg. Rate (kHz)	Ratio RP/CAEN
0-21	21.175	5.736	0.729
30-75	16.510	4.956	0.700
90-120	12.463	4.438	0.644
135-160	11.000	4.274	0.612
175-210	9.580	3.858	0.597
230-260	6.467	3.107	0.520
280-320	4.565	2.512	0.450
335-380	3.425	2.006	0.414
400-460	2.187	1.402	0.359
480-525	1.492	1.012	0.322
545-615	0.899	0.648	0.279
640-780	0.185	0.161	0.126

TABLE 4.20: Average and ratio rates of both digitizers.

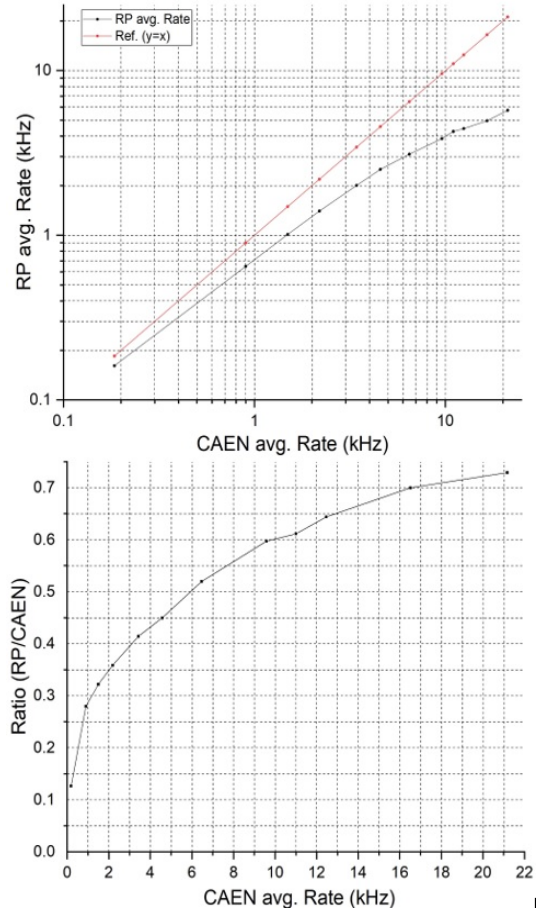

FIGURE 4.23: Rate and Ratio (RP/CAEN) vs CAEN digitizer rate.

4.6 Net neutron counting and fast neutron detection

Another fundamental set of experimental tests in this thesis project was the one concerning with the neutron detection and counting capability of the CLLB detector. For this purpose, two neutron sources were employed in the experimental setups: the ^{252}Cf, and an ^{241}Am-Be mixture source. The first test consisted in the gamma coincidence in the CLLB and a LaBr detector. the experimental setup is presented in figure 4.24. In order to have enough data to

obtain concrete and defined results, the time of these measurements were about 24 hours. The experiment was made with both neutron sources, and with the CAEN digitizer since in this test the objective was to distinguish the different response of the CLLB detector to gamma photons and neutrons.

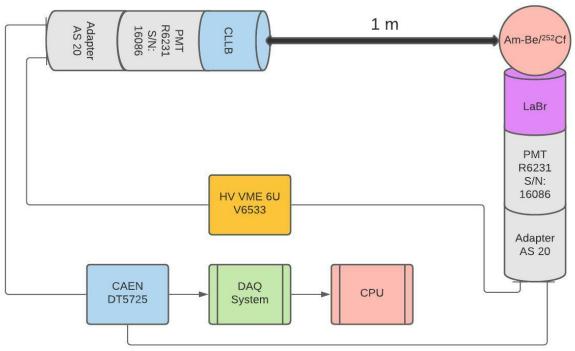

FIGURE 4.24: Experimental setup for gamma coincidence between CLLB and LaBr detectors.

As it can be observed in this diagram, the CLLB detector is set 1 meter away from the neutron source, whereas the LaBr detector is set just next to it. This test also searched for a comparison of the CLLB response before the LaBr one. The coincidence window set was 800 ns. The top plot of the figure 4.25 shows the gamma coincidence peak for the ^{252}Cf source. This neutron source was the only one used in this case because the objective was to obtain the different times in which the gamma photons and the neutrons took to reach the CLLB detector at the given distance. To calculate this, let's consider the velocity of the gamma

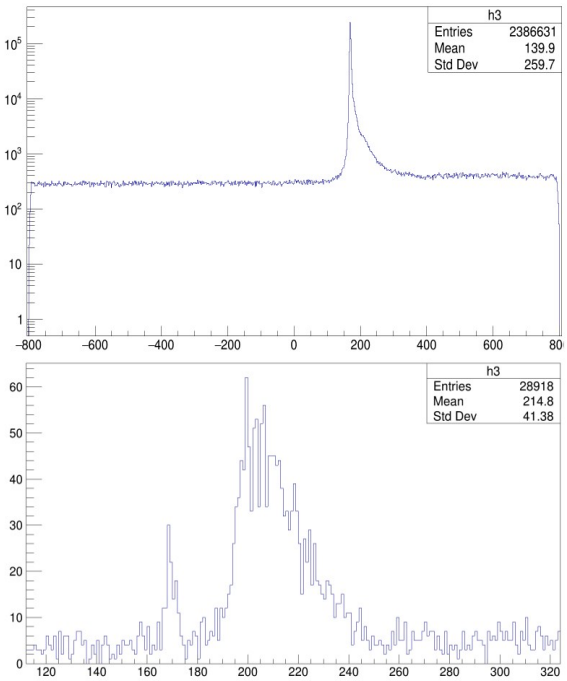

FIGURE 4.25: Gamma coincidence peak for ^{252}Cf (Top), and (bottom) time histogram for gamma (left peak) and fast neutron region (right peak).

photons (the speed of light) and the distance (1 m) between the source and the CLLB detector. With this information is possible to know that it takes about 3.33 ns for the gamma

photons to reach the detector. Now, considering a kinetic energy of 2 MeV for the neutrons, it's possible to know their velocity and hence, the time they take to reach the detector. This time is about 51.12 ns, which means that they arrived approximately 47.8 ns after the gamma photons. Observing the bottom plot of the figure 4.25, considering an approximated mean position of the gamma peak (about 170 ns), and an approximated mean position of the neutrons distribution (about 220 ns), there is a time difference of approximately 50 ns, which is very similar to the calculation performed.

In the figure 4.26 appears the response of the CLLB detector for gamma photons and neutrons for both neutron sources. The gamma region is represented by the horizontal cone-shape distribution in the two plots. Inside the green rectangle, is the region of the neutron capture and the alpha particles, which is clearer for the ^{252}Cf than for the ^{241}Am-Be source. The red rectangle encloses a region where a neutron bump appeared. These are fast neutrons that now is known, can be registered by the CLLB detector. This region is again clearer in the ^{252}Cf than in the ^{241}Am-Be source.

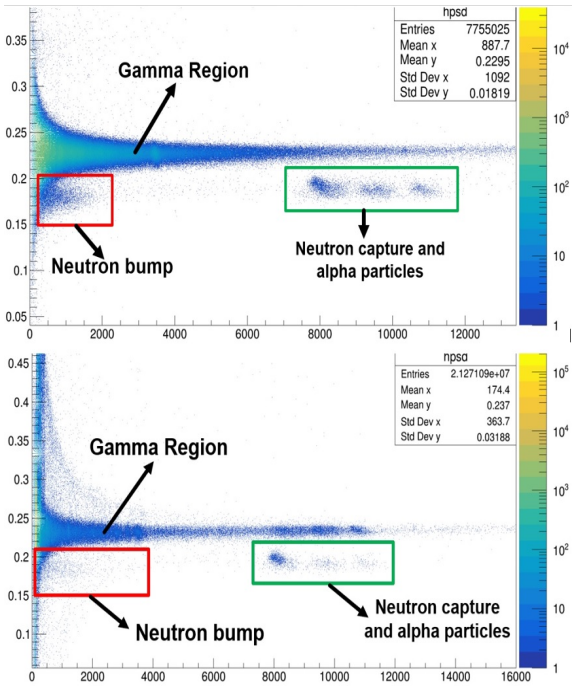

FIGURE 4.26: Gamma and neutron response of CLLB with both neutron sources. PSD histogram for ^{252}Cf (Top), and PSD histogram for ^{241}Am-Be (Bottom).

The next experimental test of this section was performed to describe with more detail the behavior of the ^{241}Am-Be source in a quantitative way. The experimental set for this purpose is shown in the figure 4.27. The Red Pitaya digitizer was used for the next measurements. An additional calibration was made in this case with ^{137}Cs, ^{60}Co, ^{22}Na, and ^{133}Ba sources without the lead and polyethylene blocks. After that, five measurements were made with the 5 cm lead block and different thicknesses of polyethilene: 0 cm (no polyethylene blocks at all), 2 cm, 4 cm, 6cm, and 8 cm. In order to generate a sufficient quantity of data, the time of each measurements was between 12 and 14 minutes.

What was found in this case is that the fast neutron counting decreased as the thickness of polyethylene increased. In contrast, the neutron captures and alpha particles increased as the polyethylene thickness did. Graphically this can be observed in the plots of figure 4.28. As it can bee seen in the plots, the region of the neutron bump (fast neutrons) is more dense for the case when there is no polyethylene blocks than when there are 8 cm of polyethylene.

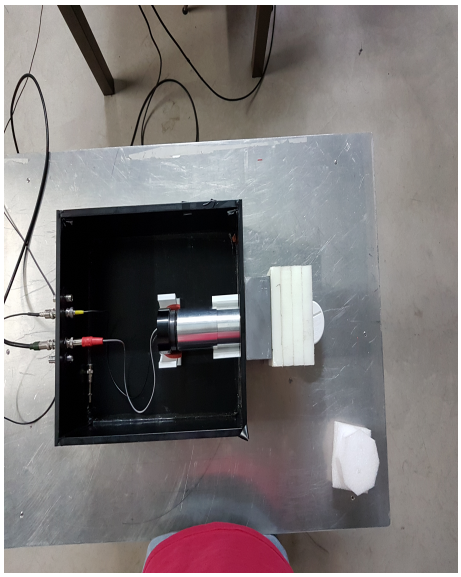

FIGURE 4.27: Experimental setup with blocks of lead and polyethylene between CLLB and ^{241}Am-Be source.

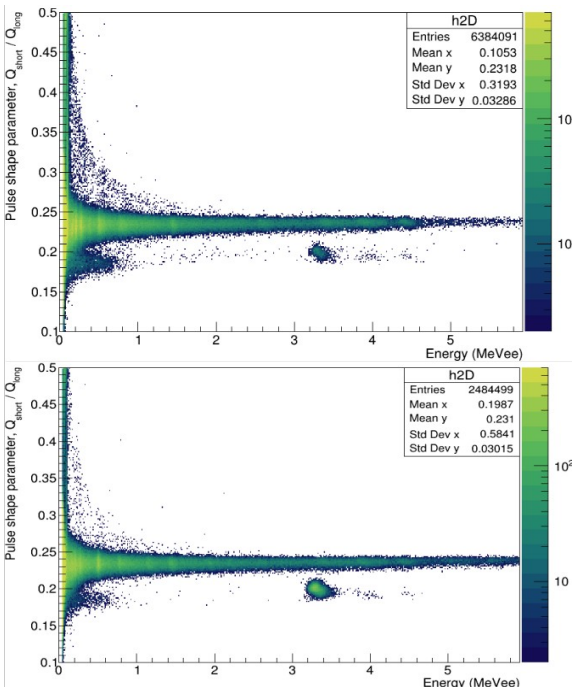

FIGURE 4.28: CLLB PSD parameter histogram for ^{241}Am-Be with a PE thickness of 0 cm (Top), and for ^{241}Am-Be with a PE thickness of 8 cm (Bottom).

By the contrary, the region previously indicated as the neutron (thermal) capture and alpha particles, appears to be more dense when there are 8 cm of polyethylene than when there are no polyethylene. This is because fast neutrons lose most of their energy while penetrating the polyethylene barrier, and then just few of them reach the detector, whereas when there are more polyethylene blocks there is more chance for neutron captures to occur.

In order to know the number of fast neutrons and neutron captures/α events, the gamma region was discriminated of the counted events employing a Root macro. Then, only the regions of interest (fast neutrons and neutron/α) were left in the PSD parameter plots. Finally, the specific measurement time was considered to obtain the number of events of interest per

second. The quantification of these phenomena is summarized in the tables 4.21 and 4.22.

PE thickness (cm)	N. of fast n (n)	Time (s)	n/s
0	15144	831.972	18.203
2	13274	848.602	15.642
4	11026	861.134	12.804
6	8012	772.687	10.369
8	6789	776.684	8.741

TABLE 4.21: Fast neutrons/s vs polyethylene thickness.

PE thickness (cm)	N. of α and n cap.	Time (s)	n/s
0	1442	831.972	1.733
2	3401	848.602	4.008
4	6301	861.134	7.317
6	7207	772.687	9.327
8	7875	776.684	10.139

TABLE 4.22: α and neutron captures/s vs polyethylene thickness.

As it was explained with the plots, the tables show how the fast neutron counting is maximum when there are no polyethylene between the ^{241}Am-Be source and the CLLB detector (18.2 counts/s), and minimum when there is the maximum polyethylene thickness (8.7 counts/s). The opposite tendency happens with the neutron capture and alpha events; the counting is minimum when there is no polyethylene (1.7 counts/s) and maximum when there is the maximum polyethykene thickness (10.139 counts/s). In both cases, the increase and decrease of counts per second have a linear behavior as it can be appreciated in the plots of figures 4.29 and 4.30.

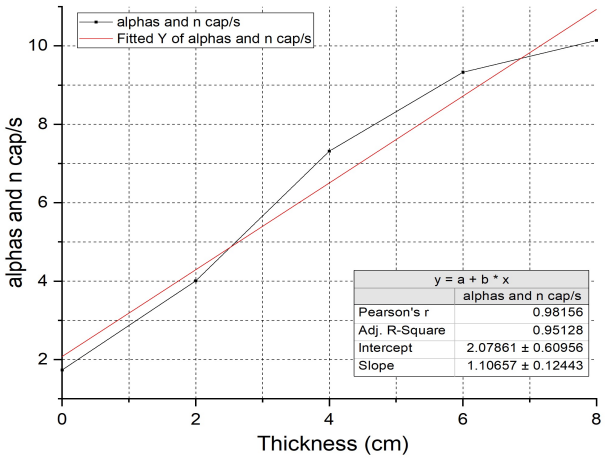

FIGURE 4.29: neutron capture/alphas per second vs thickness.

The final test of this section consisted in study the effect of the rate variation of the Red Pitaya digitizer in the neutron capture in particular. The experimental setup was the one of the figure 4.27 but only with the 5cm lead block, and setting the ^{241}Am-Be source 25 cm away from the CLLB detector. In addition, a background (no sources present) of some hours was taken in order to subtract it to each one of the rate measurements. Considering the regions already depicted in the figure 4.26, the ROOT tool *cut* was used to select the first accumulation from the left of the neutron capture and alpha region. Then, the integral of that

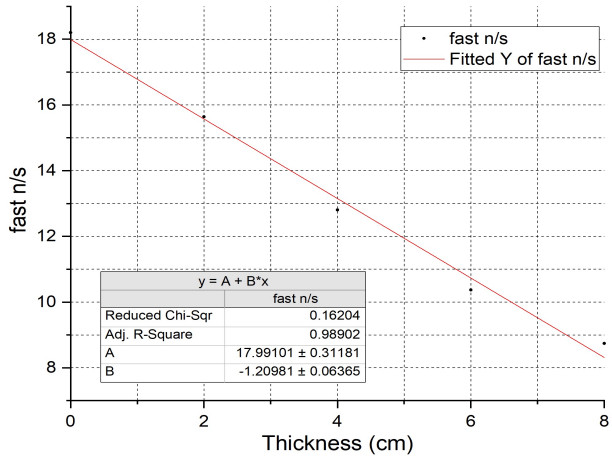

FIGURE 4.30: fast neutrons per second vs thickness.

region was calculated and divided by the time taken to make each measurement. Finally, the value obtained with the background was subtracted to each of these calculations; the results are presented in the table 4.23 and with that information the plot in figure 4.31 was obtained.

Rate (kHz)	Integral val. (I)	Test time (s)	I/s	Norm. Val.
Background	2903	8913.84	0.326	-
20	343	580.938	0.590	0.265
15	419	628.394	0.667	0.341
11	562	682.358	0.824	0.498
9	594	650.819	0.913	0.587
7	1029	913.736	1.126	0.800
5	814	616.861	1.320	0.994
4	879	629.759	1.396	1.070
2	927	599.614	1.546	1.220

TABLE 4.23: Neutron capture vs rate

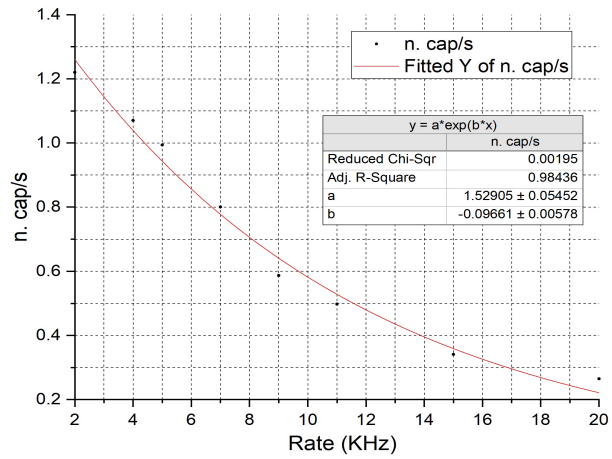

FIGURE 4.31: neutron capture vs Red Pitaya rate with ^{241}Am-Be test.

As it can be seen from the data of the table and the behavior of the plot, as the rate is increased, the neutron capture counting shows a decreasing exponential tendency. If the rate

is set in no more than 5 kHz, there is about one capture per second; after that, the counting decreases exponentially. This is an important spot to mention since in the experiment where the rates of both digitizers were compared (figure 4.23), it was precisely at a value of about 5.7 kHz, that the Red Pitaya digitizer reaches a stability level.

Chapter 5

Height and flight experiments, and additional tests with SiPM

This chapter describes further experiments focused in the physical performance of the CLLB detector inside the UAV like the one of angular efficiency depicted in the chapter 4. In this case these tests consisted in the response of the CLLB before changes of height, and also the detection capability of the plastic scintillator inside the UAV in a condition similar to a normal flight of surveillance. Finally, additional tests with SiPM coupled to CsI and SrI detectors where performed in order to observe some features of their behavior.

5.1 Height variation experiments

In the present experiment, the CLLB detector was mounted inside the UAV, which in turn was attached to a rope to be hanged up at different heights respect to the ground, where a ^{137}Cs gamma source was set. Special care was taken to position the source as much as possible right under the center of the CLLB. The Red Pitaya digitizer was also mounted on board with the detector as it can be observed in the figure 5.1.

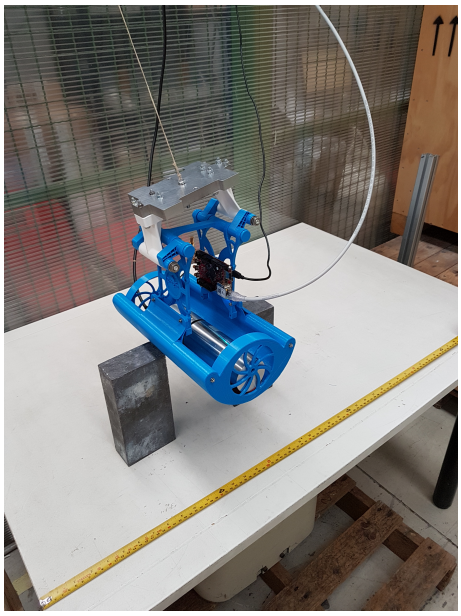

FIGURE 5.1: CLLB detector and Red Pitaya digitizer inside the UAV.

The ^{137}Cs source was chosen because its simple spectrum (just one gamma peak which is easily distinguishable compared to other sources like ^{133}Ba) allows fast and easy calculations. Four heights were considered to take the measurements: 1 m, 1.5 m, 2 m, and 2.5 m.

No measurements of heights under 1 m were taken because in a real monitoring flight this distance would be dangerous for the UAV, and hence its components. In a similar way, no measurements of heights above 2.5 m were taken because after this distance it's difficult to register a clear signal from the source. The experimental setup is shown in figure 5.2. The

FIGURE 5.2: UAV with CLLB and Red Pitaya set over the ^{137}Cs source.

UAV with the detection system inside appears at the center, and at the most superior part of the figure; whereas the ^{137}Cs source is set on the ground on a white cylindrical support in the bottom center of the figure.

As in the study of the angular efficiency in the last chapter, before performing the experimental tests, simulations in GEANT4 were made specifying the same parameters mentioned in that section (point-like source, gamma photons at 0.662 MeV with 0.85 intensity, and the distances mentioned). However, in this particular case, since the front base of the CLLB is not looking towards the source like in the simulations shown in figure 4.9, the CLLB position in these simulations had to be readjusted as it is observed in the figure 5.3. Here, it's

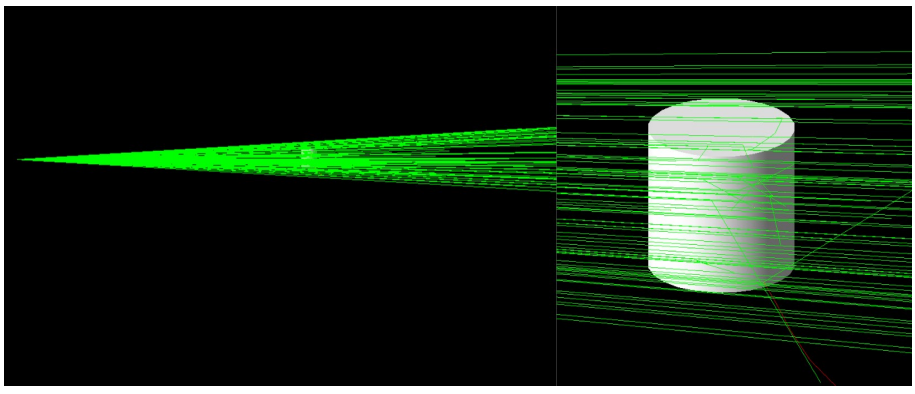

FIGURE 5.3: Experimental setup on GEANT4 for the height variations.

clear that the radiation emitted by the source reaches to the lateral face of the cylinder (CLLB detector), which is something that happens in the real experimental setup. The number of events simulated in this case was also of 4×10^7.

5.1.1 Simulation and experimental results

The simulated efficiencies at the different heights are presented in the table 5.1. As the height increases, the absolute efficiency decreases, and the error increases until a point where it turns out to be larger than the measure itself. This occurs at heights above 2 m.

Height (m)	Events (0.662 MeV)	ϵ_{abs}	Error (%)
1	7779015	0.00330	0.00036
1.5	3439836	0.00146	0.00054
2	1924476	0.00082	0.00072
2.5	1224487	0.00052	0.00090

TABLE 5.1: Simulation of ϵ_{abs} for the different heights with the ^{137}Cs source.

The experimental calculation of the peak efficiency was performed exactly in the same way as was described in the angular efficiency section in the chapter 4. The results of these measurements are shown in the table 5.2. The H_0 position was almost the same in the four measurements since there is a difference of less than 2.6% between the largest and smallest values. However, like in the case of the simulations, as the height increases the peak efficiency decreases. This is directly related with the area under the 0.662 MeV peak since it also decreases as the height increases.

Height (m)	A/bin	H_0	FWHM	ϵ_p
1	11.063	1569.911	84.618	0.00388
1.5	5.111	1568.468	84.360	0.00179
2	3.054	1609.665	87.827	0.00107
2.5	1.840	1601.845	85.159	0.00064

TABLE 5.2: Experimental efficiency ϵ_p for the different heights with the ^{137}Cs source.

As it was explained, in both cases (simulations and experimental tests) the efficiencies decreased as the height of the UAV respect to the ^{137}Cs source set on the ground increased. The comparison between both results are presented in the table 5.3. In this setup, it was expected that the difference between experiments and simulations were considerably larger compared with the differences obtained in the angular efficiency section (the smallest difference was of 14.786% at 1 m). The reason is due to the difficulty of setting the gamma source exactly under the geometrical center of the CLLB detector. Although this is relatively easy at reduced heights (1 m), it was more complicated at the largest heights because there wasn't a precise way to know that the source is actually set right under the center of the detector.

Height (m)	ϵ_{abs}	ϵ_p	Diff. (%)
1	0.00330	0.00388	14.786
1.5	0.00146	0.00179	18.436
2	0.00082	0.00107	23.364
2.5	0.00052	0.00064	18.750

TABLE 5.3: Difference between simulation and experimental results for the different heights.

In addition, the radiation is striking the detector in a different physical place (figure 4.9 and 5.3), which causes a much more reduced number of events of interest, and hence, smallest efficiency values. Nevertheless, this specific setup was necessary to know if the CLLB

detector was indeed, capable of register that type of radiation in those conditions. Finally, the plot of figure 5.4 was built with the purpose of having a graphic and more detailed view of the behavior of the simulated and experimental efficiencies respect to the change of height. As it's observed, despite the large differences between them (up to 23.364%), their behavior is very similar.

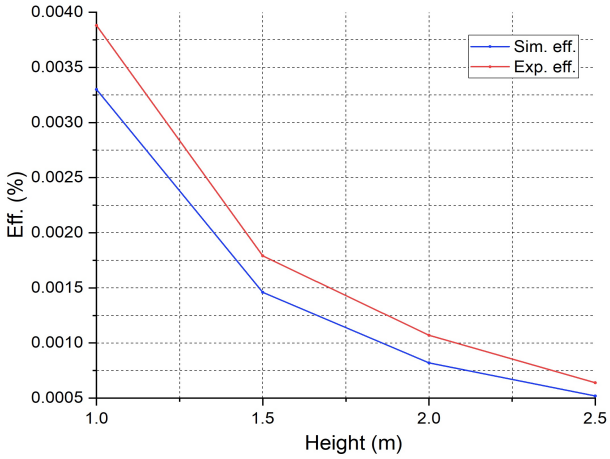

FIGURE 5.4: Plott of experimental and simulated efficiencies vs the four heights measured.

5.2 Flight experiments

The experiments developed in this section had the objective to reproduce until certain level, the conditions of a typical surveillance flight of the UAV. To achieve this purpose, the UAV with the detection system inside (CLLB + Red Pitaya) was set on a table in a sufficiently long corridor. One of the team colleagues held a ^{137}Cs source on her head while walked multiple times from side to side a distance of about 3 m and passing in front of the detector in each walk, trying as much as possible to keep the same velocity. Three different distances between the UAV and the source when this was just in front of it, were considered: 1 m, 1.5 m, and 2 m. Three measurements in each distance were performed for a total of 9 measurements. It's also important to mention that the UAV was set in the middle point of the total distance covered by the source trajectory. In order to determine the velocity of the source, each measurement was recorded in video for its analysis in the Tracker software. The experimental setup depicted can be appreciated in the figure 5.5.

The path of the source is marked with a purple straight line, and each of the blue squares represents a point (step) from which the rate of the digitizer was taken. The times and velocities obtained with the Tracker software are in the table 5.4. In general, each travel of the source didn't take more than 30 seconds, and the velocity remained below 1 m/s in all the cases except in the third measurement with a distance of 1 m between the source and the UAV. However, there were important velocity variations between the slowest and the faster travels (0.4415 m/s and 1.1060 m/s respectively).

The figures 5.6 to 5.8 show the digitizer rate vs index (steps) at distances of 1 m, 1.5, and 2 m respectively between the UAV-detector system and the source when this last is just in front of it. In all the cases it can be observed that at the central zone, the rate increases considerably respect to the rate at the beginning and the end of each of the trajectories. This behavior was expected since the central index values represent the spots where the source is closest to the UAV-detector system, whereas the index values at the beginning, and at the

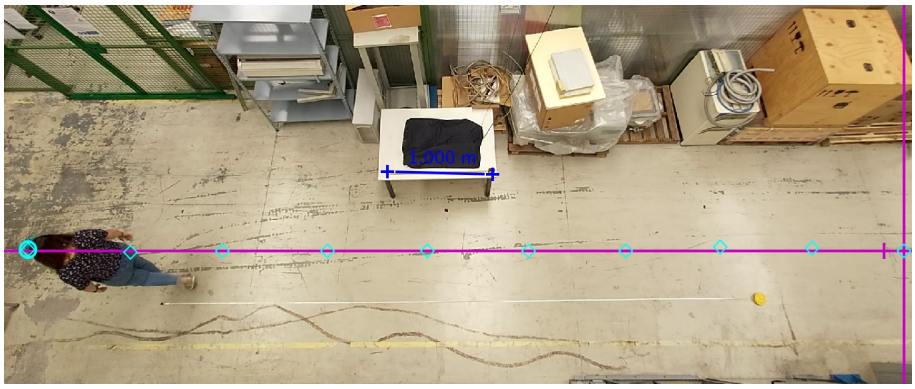

FIGURE 5.5: Experimental setup of the simulation of a surveillance flight of the UAV.

Test	Time (s)	Dist. from det. (m)	Velocity (m/s)	SD
VIDEO1	16	1	0.7425	0.0447
VIDEO2	28	1	0.4415	0.0674
VIDEO3	10.42	1	1.1060	0.0596
VIDEO4	12	1.5	0.9219	0.0324
VIDEO5	23	1.5	0.4471	0.0230
VIDEO6	15	1.5	0.7940	0.0327
VIDEO7	27	2	0.4551	0.0417
VIDEO8	15	2	0.7960	0.0606
VIDEO9	12	2	0.9760	0.0802

TABLE 5.4: Times and velocities from each of the trajectories covered by the ^{137}Cs source.

end represent the zones where the source is the furthest from the detector. Another important aspect to mention is that the maximum rate at a distance of 1 m (0.256) if considerably larger than the maximum rates obtained at distances of 1.5 and 2 m (0.124 and 0.102 respectively), which is also expected since is the closest distance between the source and the detector. In addition, even when the difference of the maximum rates at distances of 1.5 m and 2 m is low, the smallest value is at 2 m which is also expected since it's the furthest distance from the detector.

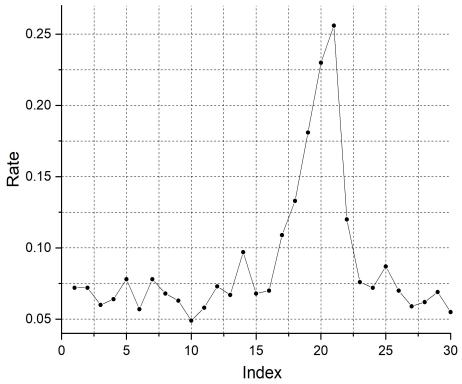

FIGURE 5.6: Red Pitaya rate vs index (steps) set by the Tracker software (1 m).

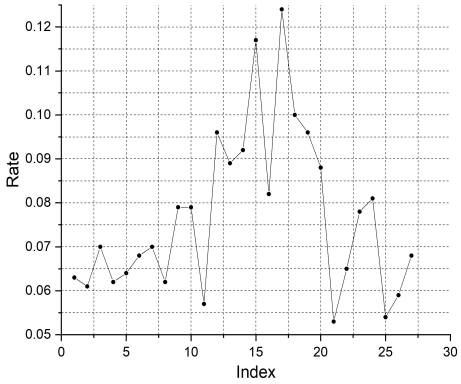

FIGURE 5.7: Red Pitaya rate vs index (steps) set by the Tracker software (1.5 m).

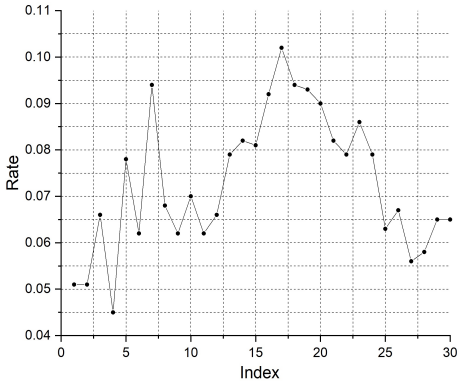

FIGURE 5.8: Red Pitaya rate vs index (steps) set by the Tracker software (2 m).

5.3 SiPM tests

The experiments with the silicon photomultiplier tubes (SiPM) had as objective to compare the resolution that could be achieved combining them with three different electronic boards, and with CsI and SrI detectors. The function of the electronic boards is to process the signal generated by the SiPM towards the Red Pitaya digitizer. The experimental setup is based on the diagram of figure 4.2, but without any structure between the radioactive source and the detectors, and with the components and systems already mentioned. The current setup used is showed in the figure 5.9. The sources used in the tests were ^{137}Cs, and ^{60}Co. As it can

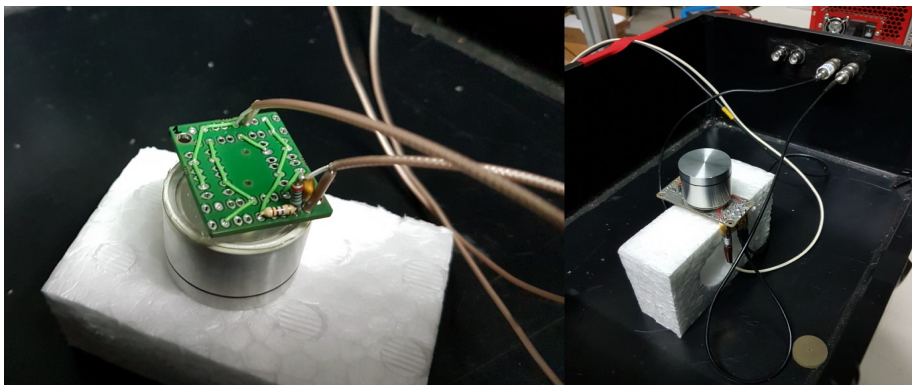

FIGURE 5.9: Experimental setup on GEANT4 for the height variations.

be seen, the SiPM matrix is coupled to the electronic board. The sources were set between

this matrix-board array and the CsI or SrI detectors. Since the SiPM are very sensitive to visible light, all the components were put inside a box to avoid an external source of noise as much as possible.

In the table 5.5 are the results of the measurements with the different board-detector combinations. The use of preamplifier, the value of the over voltage (O.V), and the source are also indicated. As in the case of the angle efficiency section, the fityk software was used to obtain the FWHM and H_0 of the gamma peaks of interest to calculate the resolution. In the case of the SrI detector, it can be appreciated that for both boards there weren't significant differences in the resolution when the values of the over voltage are changed; the largest difference was in the Trieste Board in the 1.17 MeV peak of the ^{60}Co source (about 6.3% between the minimum and maximum resolution values).

Det.	Electronic Board	O.V. (V)	Preamp.	R (^{137}Cs, 0.662 MeV)	R (^{60}Co, 1.17 MeV)	R (^{60}Co, 1.33 MeV)
SrI	Board 1	4.5	Yes	0.0787	0.0587	0.0522
		5		0.0777	0.0597	0.0515
		5.5		0.0801	0.0573	0.0506
	Trieste Board	4.5	No	0.0889	0.0566	0.0518
		5		0.0919	0.0604	0.0518
		5.5		0.0900	0.0592	0.0517
CsI	Board 2 (NUV PM)	3	yes	0.1196	0.0936	0.0788
		4		0.1118	0.1020	0.0731
		5		0.1069	0.0745	0.0675
	Board 2 (RGB PM)	2		0.1274	0.0822	0.0695
		3		0.1069	0.0683	0.0638
		4		0.1129	0.0764	0.0707

TABLE 5.5: Resolution values of the different combination board-detector.

In contrast, for the combination of the CsI detector with the two boards of the table, there are significant variations in the resolution when the over voltage value is changed. The difference in the values are between 9% and 16% (between the minimum and maximum resolutions of the same board and source), with the largest difference of almost 27% in the board with the NUV PM in the 1.17 MeV peak of the ^{60}Co source. Another important detail to observe is the fact that the resolution values were larger in all the cases with the ^{137}Cs source, and that in general, the best resolution values were for the SrI detector.

Finally, comparing the resolution values obtained in these tests with the ones obtained with the CLLB detector (table 4.19), it turned out that this last one presented better resolutions (about 0.043 with ^{60}Co source, and 0.053 with ^{137}Cs source) than the CsI and SrI detectors coupled to the SiPM. This is in fact an important evidence of the good performance of the CLLB detector and why is a proper device for the purposes of the DRAGON project.

Chapter 6

Conclusions

The CLLB inorganic scintillator detector response to gamma radiation in different physical conditions, namely the angle efficiency and the height variation efficiency tests, was very similar in the first case, to the simulations performed in the software GEANT4. The largest differences between simulations and experimental efficiencies of this section were in the case of the ^{133}Ba source, particularly in the 0.2764 MeV, and 0.3028 MeV gamma peaks. As it was already mentioned, this was due to the complex shape of these peaks, which in turn made difficult to define the area under them, generating a considerable variation respect to the simulations. However, in the rest of the gamma sources and their respective peaks analyzed, there was a good coincidence between simulation and experimental efficiency (differences not larger than 12%).

In the height variation efficiency tests, the difference respect with the simulations was more evident, specially at heights above 1.5 m. The main cause was due to the difficulty of setting the source exactly under the center of the CLLB detector. In addition, in this case the front face of the CLLB wasn't oriented directly to the direction of the source but in a different plane as it was shown in the simulations. This detail could also contribute to the reduced counting rate in the experimental tests. Despite these factors, just in one of the heights (2 m) the difference between simulation and experimental efficiencies was larger than 20%.

Talking about the neutron detection capacity and counting rate, it was observed that in fact, the CLLB detector is suitable for detecting this type of particles in different conditions like the ones depicted in the experimental setups where barriers of different materials (lead and polyethylene) were set between the neutron source and the detector. The alpha particles and neutron captures counting turned out to be directly proportional to the thickness of these barriers. An important discover during the tests with neutron sources was the fact that the CLLB detector is also capable to detect fast neutrons as it was shown in the correspondent section. It was found that the fast neutron counting is inversely proportional to the thickness of the barriers set between the neutron source and the detector.

The test that was probably the most challenging in this research, was the simulation of the UAV surveillance flight. This was because the difficulty to reproduce exactly the same conditions of motion, position, and velocity of the gamma source respect to the detection system. However, the Tracker software was very helpful in order to control as much as possible these experimental issues. Even with this level of intrinsic complexity of the experimental setup, it was possible to obtain a detector response according with what was expected to occur. The counting rate increased as the source got closer to the detection system, and decreased as it got farther. Nevertheless, even in the farthest points, the CLLB was capable to register the activity of the gamma source.

Finally, the experimental tests performed with the SiPM, the CsI and SrI detectors were useful to have a comparison between the current CLLB detector, and additional detection systems that could be potentially used in a UAV designed for the purposes of the DRAGON project. In this section, CLLB showed to be one of the best alternatives since the resolution values obtained with the same sources were better for it (5.3% with ^{137}Cs, and 4.3% for both

peaks of ^{60}Co) than for the SiPM-CsI (best value of 10.7% with ^{137}Cs and 6.38% with ^{60}Co), and SiPM-SrI (best value of 7.7% with ^{137}Cs and 5% with ^{60}Co) configurations. The main advantage of using this kind of detection systems would be their reduced size and weight, which make them a compelling alternative for the purposes of this project.

Further tests must still be performed to the DRAGON project in order to find what possible features and/or design details must or could be improved. Among the potential tests that can be carried out, it is fundamental to consider a real flight of the UAV with the detection system (CLLB + Red Pitaya digitizer) on board, and by this way, know exactly how would be the detection response to neutrons and gamma radiation. Nevertheless, the experiments developed during this thesis project have given a hopeful outlook of the expected behavior and purposes of the DRAGON project.

Bibliography

[1] *Advanced Silicon Detectors (AdvanSiD)* (2015). *ASD-RGB4S-P, ASD-NUV4S-P*, https://advansid.com

[2] BRUNELLI, D., ET AL. *DRAGoN: Drone for Radiation detection of Gammas and Neutrons*, Department of Physics and Astronomy "Galileo Galilei", University of Padova, Padova. IEEE, 2020.

[3] CAEN ELECTRONIC INSTRUMENTATION (2016). *User Manual UM3148 DT5730/DT5725 8-Channel 14-bit 500/250 MS/s Digitizer8-Channel 14-bit 500/250 MS/s Digitizer*, www.Manualslib.com

[4] CHEREPY, N.J. *History and Current Status of Strontium Iodide Scintillators*, Lawrence Livermore National Laboratory, Livermore, CA 94550, September 2017.

[5] FONTANA, C., ET AL. *A distributed data acquisition system for signal digitizers with on-line analysis capabilities*, Department of Physics and Astronomy "Galileo Galilei", University of Padova, Padova. IEEE, 2017.

[6] HAMAMATSU *Photomultiplier tubes and assemblies for scintillation counting and high energy physics*, www.hamamatsu.com. Japan: September 2012.

[7] KNOLL, G. *Radiation Detection and Measurement*, third edition. New York: John Willey & Sons, Inc. 2000.

[8] LEO, W. *Techniques of Nuclear and Particle Physics Experiments. A How-to approach*, Berlin: Springer-Verlag, 1987.

[9] PINO, F., ET AL. *Characterization of a medium-size CLLB scintillator and its potential use in an unmanned airborne radiation monitoring system*, Department of Physics and Astronomy "Galileo Galilei", University of Padova, Padova. 2020.

[10] PINO, E. *Development of Innovative Technology for Detection and Identification of Radioactive Materials*, Universitá Degli Studi di Padova, Dipartamento di Física ed Astronomía "Galileo Galilei", Scuola di Dottorato di Ricerca in Física. Dottorato in Cotutela, September 2014.

[11] RED PITAYA STEMLABS. (2021). *Oscilloscope and Signal Generator specifications*, https://www.redpitaya.com/f145/specifications

[12] SAINT-GOBAIN CRYSTALS. (2021). *CLLB dual gamma/neutron scintillator*, https://www.crystals.saint-gobain.com/products/cllb

[13] SHU, B.. (2015). *National Nuclear Data Center*, Brookhaven National Laboratory, https://www.nndc.bnl.gov/nudat2/